Investigation of the dB/dH effect using trapped flux in type-II superconductors

M. A. R. LeBlanc, Sean X. Wang, David LeBlanc, Martin Krzywinski, and Jinglei Meng
Physics Department, University of Ottawa, Ottawa, Canada K1N 6N5
(Received 10 November 1994; revised manuscript received 19 January 1995)

We show that the dB/dH effect (i.e., a "discontinuity" in the B profile) should manifest itself quite dramatically in plots of $\langle B\rangle_{\rm rem}/\langle B\rangle_{\rm in}$ vs either $\langle B\rangle_{\rm in}$ or vs $\langle B\rangle_{\rm rem}$. Here $\langle B\rangle_{\rm in}$ is the magnetic-flux density permeating the zero-field-cooled specimen in the presence of an applied magnetic field H_a and $\langle B\rangle_{\rm rem}$ is the remanent magnetic-flux density after H_a has been removed. Our data on the five materials we have investigated (two weak pinning, two intermediate, and one strong pinning low-T_c type-II superconductors) graphed in these discriminating formats show no evidence of a dB/dH effect.

I. INTRODUCTION

Many workers[1–11] postulate that a steep descent of the magnetic-flux density occurs over a distance of the order of the penetration depth λ at the boundary of the flux-line lattice penetrating into a flux-free but not pinning-free type-II superconductor. Consequently, the configuration of the magnetic-flux density (the B profile) on a macroscopic scale relative to λ is depicted with a "discontinuity" along the front of the advancing flux profile. The magnitude of this discontinuity in the B profile is generally regarded to correspond to $B_{c1}=\mu_0 H_{c1}$, where H_{c1} is the lower critical field. This feature has been denoted the dB/dH effect.[12–14]

In this paper we report on a search for the signature of such a discontinuity in the remanent (residual) magnetic flux $\phi_{\rm rem}$ trapped in bulk type-II superconductors. In our work, the flux is trapped by subjecting the virgin (i.e., zero-field-cooled) specimen to an isothermal application and removal of a uniform magnetic field H_a directed along its length. The peak value of H_a during each such cycle is denoted $H_{\rm cycle}$. The sample is zero-field cooled before each cycle. This simple procedure has been exploited by many workers. The standard approach has been to display $\phi_{\rm rem}$ or, equivalently, its spatial average $\langle B\rangle_{\rm rem}$ vs $H_{\rm cycle}$.[15–22] However, as we will demonstrate in some detail, the signature of a discontinuity (dB/dH effect) does not emerge clearly in this standard approach. One reason is that the modeling of $\phi_{\rm rem}$ vs $H_{\rm cycle}$ involves "extraneous" components which need to be separately identified. This aspect is developed further in this article.

In our work, in order to circumvent this problem, we not only determine $\phi_{\rm rem}$ vs $H_{\rm cycle}$, but we also measured $\phi_{\rm in}$ the magnetic flux permeating the specimen, hence $\langle B\rangle_{\rm in}$, its spatial average, when H_a attains the peak of its excursion. The evolution of $\phi_{\rm rem}$ and $\phi_{\rm in}$ with respect to each other then constitutes the "raw" data for our analysis and our search for evidence of a dB/dH effect. First, we explore graphs of $\langle B\rangle_{\rm rem}$ vs $\langle B\rangle_{\rm in}$ and show that these contain more pertinent information and fewer independent ingredients than graphs of $\langle B\rangle_{\rm rem}$ vs $H_{\rm cycle}$. Although a dB/dH effect comparable to B_{c1} will emerge clearly in such graphs for weak pinning materials, a dB/dH effect which is a small fraction of B_{c1} can, however, escape notice. Consequently, we examined alternative representations of the data.

We show that plots of the ratio $\langle B\rangle_{\rm rem}/\langle B\rangle_{\rm in}$ vs either $\langle B\rangle_{\rm in}$ or $\langle B\rangle_{\rm rem}$ can, however, quite dramatically reveal the existence of a dB/dH effect if such an effect is present. Nevertheless, our data, displayed in these sensitive and discriminating formats, show no evidence for a dB/dH effect in any of our samples.

This lack of corroboration of a dB/dH effect from our data is noteworthy since we have focused on specimens where B_{c1} is comparable to or greater than $\langle B\rangle_{\rm rem\,max}$, the saturation remanent magnetic-flux density. Under these circumstances the contribution of a dB/dH effect is expected to emerge clearly unless it is a minute faction of B_{c1}. For completeness, we have also pursued measurements on a relatively strong pinning material, i.e., where $\langle B\rangle_{\rm rem\,max}\gtrsim B_{c1}$. In this sample, the dB/dH tends to be masked by the steep gradients in the B profiles associated with the large bulk critical current density. As expected, this sample carries no signature of the dB/dH effect.

II. EXPERIMENTAL ARRANGEMENT AND PROCEDURE

We present measurements on five materials and two different geometries. The composition, geometry, dimensions, estimated lower critical field H_{c1}, and the measured $\langle B\rangle_{\rm rem\,max}=\mu_0\langle M\rangle_{\rm rem\,max}$, the spatial average of the maximum remanent trapped flux, are listed in Table I. The NbTa, PbIn, and NbZr samples each consisted of a bundle of a dozen straight insulated wires set in epoxy. The Nb sample comprised six parallel ribbons separated by thin Mylar sheets

TABLE I. Composition, dimensions, H_{C1} and $\langle M\rangle_{\rm rem}$ of samples.

Sample	Length (cm)	Radius	$\mu_0 H_{c1}$ (mT)	$\mu_0\langle M\rangle_{\rm rem}$ (mT)
$Pb_{0.86}In_{0.14}$	4	0.0625	20	22
$Pb_{0.45}Bi_{0.55}$	6	0.25	25	56
Nb (ribbon)	4	0.025×1.0	120	95
$Nb_{0.5}Ta_{0.5}$	4	0.0625	30	50
Nb Zr	6	0.013	50	≥350

 © 1995 The American Physical Society

and set in epoxy. The radius or thickness given in the table refer to the constituent wire or ribbon. A single layer noninductively (bifilar) wound 38BS Manganin wire heater intimately embraces the length of the samples. Several layers of masking tape provide a thermal barrier between the heater and the ambient 4.2-K helium bath.

A main pickup coil embraces the waist of the specimen and is series opposition connected to a pair of identical balancing pickup coils, one placed above and the other below the central coil. The balancing coils do not embrace the sample, but are threaded by the applied magnetic field H_a provided by a long superconducting solenoid. The latter, 17.5 cm long, with an inner radius of 2.0 cm and outer radius of 3.0 cm, is wound with multifilamentary 0.040-cm-diam Supercon NbTi wire. The residual field of the solenoid is $\lesssim 0.1$ mT after a sweep of 0.5 T.

The balanced pickup coil feeds an electronic amplifier integrator which drives the Y axis of an XY recorder. The X axis is driven by a signal proportional to H_a from a calibrated shunt traversed by the current I fed to the solenoid by a battery-driven, hence ripple-free transistorized power supply.

The specimen is zero-field cooled prior to each measurement. The magnetic flux permeating the specimen is continuously monitored as H_a is slowly raised to a selected peak value, denoted H_{cycle}, and then gradually removed [see Fig. 1(a)]. The duration of such a cycle is generally proportional to H_{cycle} and typically ≈ 1 min for $\mu_0 H_{\text{cycle}} \approx 0.1$ T. After the cycle of H_a is completed, the temperature of the specimen is raised from 4.2 K to above T_c. The remanent magnetic flux is thereby released and directly detected by the pickup coil-amplifier-integrator-recorder system. The locus of the trace on the XY recorder returns to its initial position when no electronic drift has occurred during the entire sequence just described. Tracings which do not close are rejected.

The system is calibrated on the standard assumption that the virgin (zero-field-cooled) specimen allows no penetration of flux when H_a is applied from zero in the low-field range where $H_a \ll H_{c1}$. Under these circumstances the response of the system, hence the XY recorder trace versus H_a, is linear.

We have exploited two modes of measurement in our investigation. In one mode $\langle B \rangle = \phi/A$, the spatial average of the magnetic flux ϕ permeating the specimen is continuously monitored vs H_a. Here A is the cross section of the sample. In the other mode, the magnetization $\mu_0 \langle M \rangle = \langle B \rangle - \mu_0 H_a$ is continuously monitored vs H_a. The tracings corresponding to these two modes are sketched in Fig. 1. The mode is determined by the type of balancing selected in the construction of the pickup coil assembly. For the $\langle B \rangle$ vs H_a display, NS, the product of the number of turns N and area S embraced by the balancing coils is carefully adjusted so that the detection system generates no signal when $H_a < H_{c1}$ is applied to the zero-field-cooled sample in the superconducting state. For the $\langle M \rangle$ vs H_a curves, NS is chosen so that the detecting system generates no signal when no sample is present or equivalently when the specimen is maintained above T_c by means of the heater.

III. BACKGROUND

Although the dB/dH effect is frequently introduced in the analysis of magnetic phenomena in the bulk of type-II

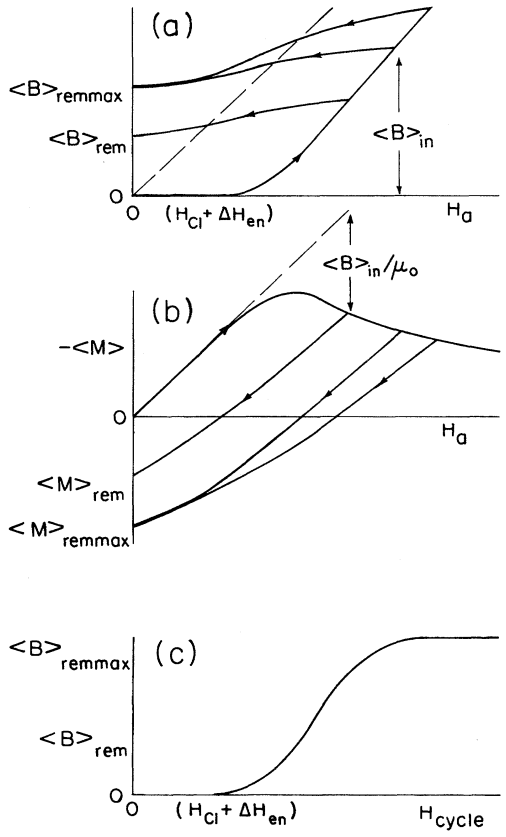

FIG. 1. (a) Schematics displaying the evolution of $\langle B \rangle$, the spatial average of the magnetic-flux density permeating the specimen, as the applied magnetic field H_a is impressed after zero-field cooling and reduced to zero when arbitrary values, denoted H_{cycle}, are attained. When H_{cycle} exceeds a threshold value, denoted H_{plateau}, the remanent magnetic-flux density trapped in the specimen, $\langle B \rangle_{\text{rem}} = \mu_0 \langle M \rangle_{\text{rem}}$, reaches a maximum (saturation) level, denoted $\langle B \rangle_{\text{rem max}} = \mu_0 \langle M \rangle_{\text{rem max}}$ and remains constant at this magnitude for $H_{\text{cycle}} > H_{\text{plateau}}$. When $H_a \leq (H_{c1} + \Delta H_{\text{en}})$, no magnetic flux is observed to enter the specimen; hence, $\langle B \rangle_{\text{rem}} = 0$. In our work, we continuously monitored such curves and hence determined $\langle B \rangle_{\text{rem}}$ vs $\langle B \rangle_{\text{in}}$, where $\langle B \rangle_{\text{in}}$ denotes the value of $\langle B \rangle$ at H_{cycle}. (b) Schematic displaying the evolution of the magnetization $\langle M \rangle = (\langle B \rangle - \mu_0 H_a)/\mu_0$ as H_a is applied after zero-field cooling and reduced to zero after attaining arbitrary values denoted H_{cycle}. When $H_a \leq (H_{c1} + \Delta H_{\text{en}})$ no residual magnetization is observed. When H_{cycle} exceeds the threshold value H_{plateau}, $\langle M \rangle_{\text{rem}}$ attains a maximum magnitude denoted $\langle M \rangle_{\text{rem max}} = \langle B \rangle_{\text{rem max}}/\mu_0$. In our work we also continuously monitored such curves. Note that (a) and (b) are complementary and equivalent data curves which can be obtained by suitably adapting the balancing of the pickup coil arrangement in our monitoring setup. (c) Schematic display of plots of $\langle B \rangle_{\text{rem}} = \mu_0 \langle M \rangle_{\text{rem}}$ vs H_{cycle}, which can be determined from either graphs of (a) or (b) above. Note, however, that neither (a) nor (b), hence such detailed data on the evolution of $\langle B \rangle$ or $\langle M \rangle$ vs H_a, is required to construct the graph depicted above in (c). The crucial feature of our work is that we monitored both (a) and (b) and thereby determined both $\langle B \rangle_{\text{in}}$ and $\langle B \rangle_{\text{rem}}$ vs H_{cycle}.

superconductors,[1–13] our search of the literature revealed no direct experimental evidence supporting this concept. Our purpose in this paper is not to examine the theoretical basis of the dB/dH effect but to explore evidence of its existence. Ullmaier[12] has reviewed this idea in some detail. For completeness, we present a brief outline of his discussion.

The driving Lorentz force density $\vec{F}_L=\vec{j}\times\vec{B}$ in the static critical state of a flux-line lattice is in equilibrium with the pinning force density $\vec{F}_P(B)$. For an infinite slab with thickness along the x axis, the current density $\vec{j}$ along y, and the magnetic flux density $\vec{B}$ along z, this equilibrium condition reads

$$-j_y B_z = F_P . \tag{1}$$

Introducing Maxwell's equation $\nabla\times\vec{H}=\vec{j}$ for planar geometry leads to

$$B_z \frac{dH_z}{dx} = F_P . \tag{2}$$

The dB/dH effect is introduced by (i) rewriting the current density in the form

$$-j=\frac{dH}{dx}=\frac{dH}{dB}\frac{dB}{dx}=\frac{1}{(dB/dH)}\frac{dB}{dx} \tag{3}$$

(where we have neglected the subscripts) and (ii) interpreting the quantity dB/dH and its inverse dH/dB as follows.

In the Abrikosov[23] theory, the Ginzberg-Landau parameter κ and the thermodynamic critical field H_c dictate the equilibrium between the flux-line density B and the magnetic field H in ideal (pinning-free) type-II superconductors. Several authors have proposed[13,24–26] that the relationship between B and H for the corresponding κ and H_c remains effective when pinning is introduced in the material. Since dH/dB, denoted $(dH/dB)_{\rm rev}$ in the reversible material, is very small when B is in the range $0\leq B<\mu_0 H_{c1}$, the gradient of the B profile,

$$\frac{dB}{dx}=\frac{F_p(B)}{B}\left(\frac{dB}{dH}\right)_{\rm rev}=\frac{F_p(B)}{B}\Big/\left(\frac{dH}{dB}\right)_{\rm rev}, \tag{4}$$

is then expected to be very steep inside the bulk of the nonideal (irreversible) specimen when the flux-line density falls in the range $0<B(x)\lesssim\mu_0 H_{c1}$. The region where this steep gradient occurs is regarded as occupying a thickness comparable to the penetration depth λ. Hence this region constitutes a near discontinuity in the B profile of weak-pinning bulk specimens where dimensions are very large compared with λ.

The presence of such a discontinuity in the B profile should play a significant role in the evolution of the magnitude of the magnetic moment of materials with large H_{c1} and weak pinning during the initial application H_a as illustrated in Fig. 2(e) and in the amount of flux retained by the samples after H_a has been removed as illustrated in Fig. 2(e). Consequently, in our investigation we have focused on specimens exhibiting relatively weak pinning and an appreciable H_{c1}.

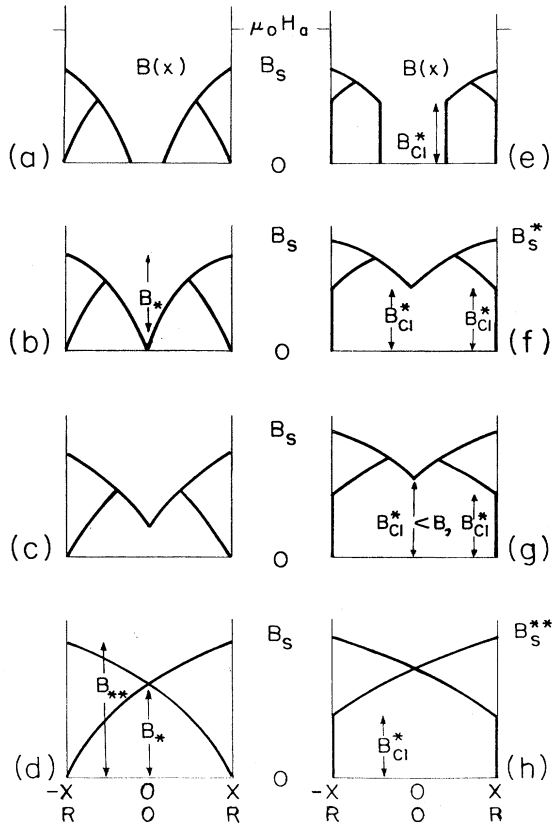

FIG. 2. Schematic displays of the evolution of the critical B profiles in an infinite slab or cylinder as a function of B_S, the magnetic-flux density just *inside* the surface of the specimen when $H_a=H_{\rm cycle}$ (upper curves) and subsequently when $H_a=0$ (lower curves in each drawing). The sketches without [with] a discontinuity, i.e., a dB/dH effect of magnitude B^*_{c1}, are shown in (a), (b), (c), and (d) [(e), (f), (g), and (h)]. The quantities B_*, B_{**}, B^*_S, and B^{**}_S illustrated in the sketches are discussed in the text. Expressions for $\langle B\rangle_{\rm in}$ and $\langle B\rangle_{\rm rem}$ vs B_S are developed in the Appendix.

IV. RESULTS AND DISCUSSION

A. Standard format: $\langle M\rangle_{\rm rem}=\langle B\rangle_{\rm rem}/\mu_0$ vs $H_{\rm cycle}$

Throughout the literature, since the earlier work of Goedemoed *et al.*,[15] the remanent magnetization $\langle M\rangle_{\rm rem}$ generated by a sweep of H_a has been plotted as a function of $H_{\rm cycle}$, the peak value attained by H_a during an excursion.[7,16–22] The resulting "universal" curve is displayed schematically in Fig. 1(c), and exhibits three distinct features:[18] (i) A low-field region where $\langle M\rangle_{\rm rem}=0$ over a range $0<H_{\rm cycle}<H_{\rm threshold}$ and (ii) an S-shaped section followed by (iii) a plateau whose edge is denoted $H_{\rm plateau}$. Let $\langle M\rangle_{\rm rem\,max}$ denote the value of $\langle M\rangle_{\rm rem}$ at the plateau.

The applied magnetic flux is excluded from the bulk by the Meissner screening current I_M when $H_{\rm cycle}<H_{c1}$. Several workers have proposed that $H_{\rm threshold}$ may appreciably exceed H_{c1} due to strong surface pinning,[27–30] the action of image forces,[31] and/or other mechanisms.[32,33] Letting $\Delta H_{\rm en}(H_a)$ denote the surface barrier against flux entry resulting from these properties, we write

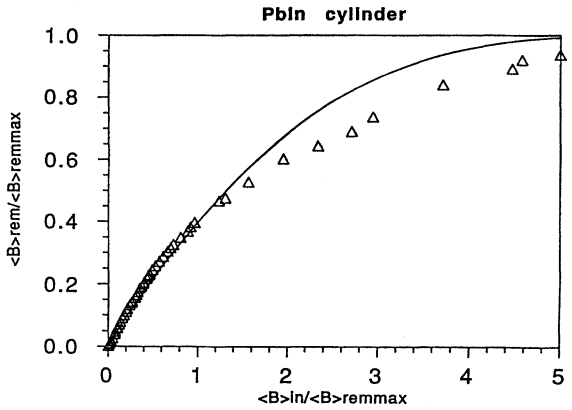

FIG. 3. $\langle B\rangle_{\mathrm{rem}}$, the remanent magnetic-flux density trapped in the specimen at $H_a=0$ after an excursion of H_a to a value denoted H_{cycle}, vs $\langle B\rangle_{\mathrm{in}}$, the spatial average of the magnetic-flux density permeating the specimen at the corresponding $H_a=H_{\mathrm{cycle}}$. Both quantities are normalized with respect to the maximum (saturation) remanent flux density $\langle B\rangle_{\mathrm{rem\ max}}$. The sample was zero-field cooled before each measurement. The solid curve was calculated using $j_c=\alpha$, where α is a constant (i.e., Bean approximation) and assuming no discontinuities in the B profiles (i.e., no dB/dH effect). The equations are developed in the Appendix.

$$H_{\mathrm{threshold}}=H_{c1}+\Delta H_{\mathrm{en}}. \tag{5}$$

When H_{cycle} rises above $H_{\mathrm{threshold}}$, the depth of penetration of magnetic flux into the specimen is determined by j_c, the bulk critical current density, and $B_S(H_a)$, the magnetic-flux density a distance of the order of the penetration depth inside the specimen as sketched in Fig. 2. The magnitude of the Meissner current $I_M(H_a)$ and of the surface barrier $\Delta H_{\mathrm{en}}(H_a)$ govern the evolution of B_S as H_a increases. The relation between the latter can be written

$$\frac{B_S(H_a)}{\mu_0}=H_a-I_M(H_a)-\Delta H_{\mathrm{en}}(H_a). \tag{6}$$

Here $I_M=M_{\mathrm{rev}}$, the magnitude of the reversible Abrikosov diamagnetic magnetization.

The total magnetic flux initially permeating the specimen increases as $H_a>H_{\mathrm{threshold}}$; hence, B_S is increased (see Fig. 2). Consequently, the amount of flux trapped in the sample after $H_a=H_{\mathrm{cycle}}$ has been removed (see Fig. 2) also rises and traces the S-shaped curve of Fig. 1(c).

The growth in the remanent trapped flux ceases when $H_{\mathrm{cycle}}=H_{\mathrm{plateau}}$ and the corresponding B_S attains a level denoted B_S^{**} (see Fig. 2). For $H_{\mathrm{cycle}}\geq H_{\mathrm{plateau}}$ and $B_S\geq B_S^{**}$, the remanent B profile exists in a saturated critical state where the entire specimen is filled with flux-retaining critical currents; hence, $\langle B\rangle_{\mathrm{rem}}=\langle B\rangle_{\mathrm{rem\ max}}=\mu_0\langle M\rangle_{\mathrm{rem\ max}}$.

Modeling of $\langle M\rangle_{\mathrm{rem}}$ vs H_{cycle} over the S-shaped region of Fig. 1(c) requires complementary information regarding the dependence of both $I_M(H_a)$ and $\Delta H_{\mathrm{en}}(H_a)$ on $H_a=H_{\mathrm{cycle}}$. Thus four quantities [$I_M(H_a)$, $\Delta H_{\mathrm{en}}(H_a)$, $j_c(B)$, and dB/dH] play a role in the detailed structure of the S-shaped region. Consequently, unambiguous evidence for the dB/dH effect is difficult to obtain from $\langle M\rangle_{\mathrm{rem}}$ vs H_{cycle} curves.

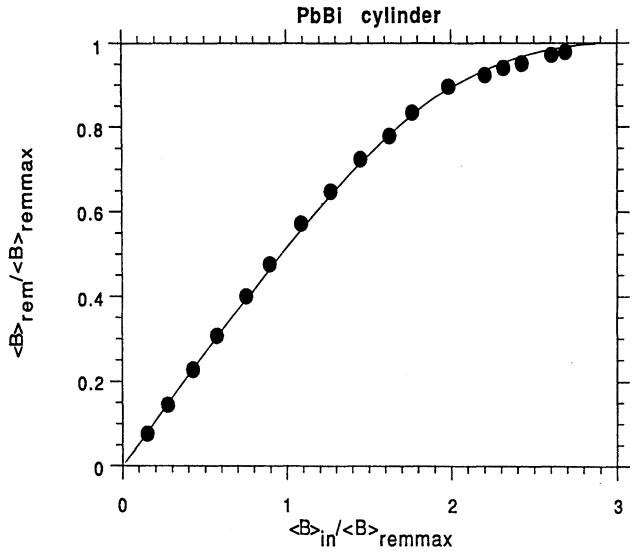

FIG. 4. $\langle B\rangle_{\mathrm{rem}}/\langle B\rangle_{\mathrm{rem\ max}}$ vs $\langle B\rangle_{\mathrm{in}}/\langle B\rangle_{\mathrm{rem\ max}}$. The solid curve was calculated using $j_c=\alpha/(B+B_0)$ with $B_0=0.35B_*=0.35\sqrt{2\mu_0\alpha R}$. Again, we assumed no discontinuities in the B profiles (i.e., no dB/dH effect).

B. Alternative approach: $\langle B\rangle_{\mathrm{rem}}$ vs $\langle B\rangle_{\mathrm{in}}$

In order to circumvent the difficulties just mentioned, we have explored the merits of measuring and plotting $\langle B\rangle_{\mathrm{rem}}=\mu_0\langle M\rangle_{\mathrm{rem}}$ vs $\langle B\rangle_{\mathrm{in}}$, the spatial average of the magnetic-flux density initially permeating the specimen when $H_a=H_{\mathrm{cycle}}$. This procedure, in effect, replaces $B_S(H_a)$, a quantity which is only indirectly accessed, by $\langle B\rangle_{\mathrm{in}}$, which is directly measured. The quantities $\langle B\rangle_{\mathrm{rem}}$ and $\langle B\rangle_{\mathrm{in}}$ are parametrically linked via $B_S(H_a)$. The dependence of $B_s(H_a)$ on H_a, however, plays no role in the modeling of $\langle B\rangle_{\mathrm{rem}}$ and $\langle B\rangle_{\mathrm{in}}$. Consequently, no supplementary input for $I_M(H_a)$ and $\Delta H_{\mathrm{en}}(H_a)$ is involved in this approach. Figures 3–7 display our experimental results and corresponding theoretical curves in this format. For convenience, $\langle B\rangle_{\mathrm{rem}}$

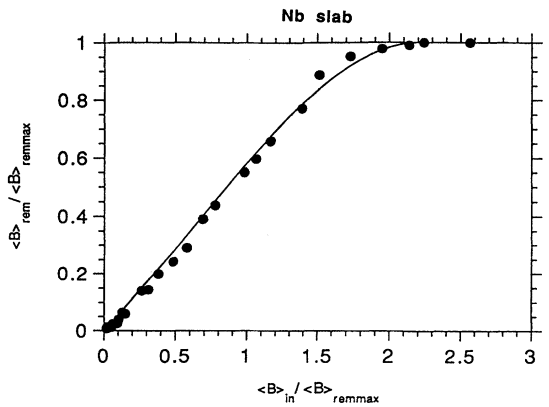

FIG. 5. $\langle B\rangle_{\mathrm{rem}}/\langle B\rangle_{\mathrm{rem\ max}}$ vs $\langle B\rangle_{\mathrm{in}}/\langle B\rangle_{\mathrm{rem\ max}}$. The solid curve was calculated using $j_c=\alpha/(B+B_0)$ with $B_0=0.4B_*=0.4\sqrt{2\mu_0\alpha X}$. Again, we assume no discontinuities in the B profiles (i.e., no dB/dH effect).

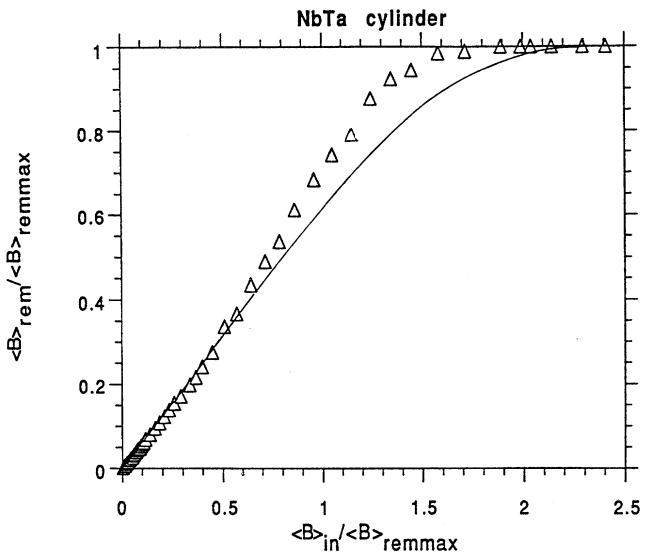

FIG. 6. $\langle B\rangle_{\rm rem}/\langle B\rangle_{\rm rem\,max}$ vs $\langle B\rangle_{\rm in}/\langle B\rangle_{\rm rem\,max}$. The solid curve was calculated using $j_c=\alpha/(B+B_0)$ with $B_0=0.15B_*$. Again, we assumed no discontinuities in the B profiles (i.e., no dB/dH effect).

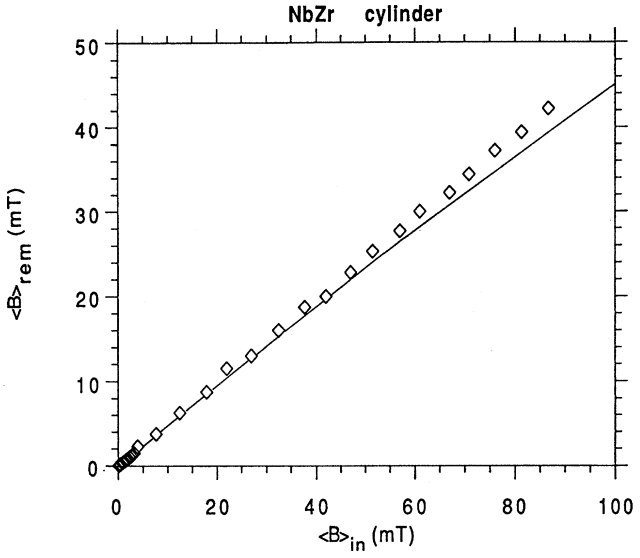

FIG. 7. $\langle B\rangle_{\rm rem}$ vs $\langle B\rangle_{\rm in}$. The data are not normalized with respect to $\langle B\rangle_{\rm rem\,max}$ since we could not determine with certainty that a saturation value (plateau) of $\langle B\rangle_{\rm rem}$ had been established by the excursions to the maximum $\mu_0 H_{\rm cycle}\approx 0.7$ T available in the measurements. To ensure a negligible residual field, the long solenoid used in this work comprised only two layers of 0.025-cm-diam multifilamentary NbTi wire; hence, our current source could not provide sufficient current and hence sufficient magnetic field to map out the plateau of $\langle B\rangle_{\rm rem}$ vs $H_{\rm cycle}$. The solid curve was calculated using $j_c=\alpha$. Again, we assumed no discontinuities in the B profiles (i.e., no dB/dH effect).

and $\langle B\rangle_{\rm in}$ are normalized to $\langle B\rangle_{\rm rem\ max}$, the spatial average of the maximum or saturation remanent flux trapped at the plateau. We note that "excellent" agreement is obtained between the calculated curves and observations with no dB/dH effect coming into play, hence taking B_{c1}^*, the magnitude of the discontinuity in the B profile, equal to zero.

From inspection of Fig. 2, we expect that the initial slope of curves of $\langle B\rangle_{\rm rem}$ vs $\langle B\rangle_{\rm in}$ should be close to unity, if the dB/dH effect is playing a role. The initial slopes for all of our data curves, however, are near $\frac{1}{2}$. In order to assess quantitatively the accuracy of this format to clearly reveal the presence or absence of a dB/dH effect, it is instructive to model the evolution of $\langle B\rangle_{\rm in}$ vs $\langle B\rangle_{\rm rem}$ for basic geometries, different dependences of j_c on B, and with discontinuities in the B profiles (dB/dH effects) of various magnitudes relative to the bulk pinning contribution.

We have pursued this exercise for idealized infinite slab and cylinder geometries.

For simplicity, we focused on the following well-known form for the dependence of j_c on B:

$$j_c=\frac{\alpha}{(B+B_0)^n}, \tag{7}$$

where α, B_0, and n are adjustable parameters.

This function leads to simple analytic expressions for $\langle B\rangle_{\rm in}$ and $\langle B\rangle_{\rm rem}$ vs B_S, which are developed in the Appendix. It is convenient to scale B_S, B_0, and B_{c1}^*, with respect to a parameter, denoted B_*, which reads

$$B_*^{n+1}=\mu_0(n+1)\alpha X=\mu_0(n+1)\alpha R, \tag{8}$$

where X is the half-width of the slab and R is the radius of the cylinder. We note that in our analysis B_* corresponds to the first full penetration field only when both B_0 and B_{c1}^* are zero.

We stress that taking $n>0$ and $B_0=0$ in Eq. (7), allows j_c to become very large when B is small. Consequently, the B profile at the boundary with a flux-free region will display a steep rise on a macroscopic scale even without the intervention of the dB/dH effect. For this reason it is instructive to examine this special situation in some detail. We refer to the special case where $n=1$ and $B_0=0$, hence $j_c=\alpha/B$, as the simple Kim approximation.[34] Frequently, j_c is considered to be independent of B over the range under consideration. This will be denoted the Bean approximation[35] and constitutes a special case of Eq. (7) where $n=0$. These two approximations bracket a wide spectrum of dependences of j_c on B. Consequently, we focus on these two cases to explore the sensitivity of the modeling to variations in the dependence of j_c on B. We note that the introduction of the parameter B_0 into $j_c=\alpha/(B+B_0)$ and allowing B_0 to increase relative to B_* transforms the dependence of j_c on B from the simple Kim case toward the Bean approximation.[36]

Figures 8 and 9 display families of theoretical curves of $\langle B\rangle_{\rm rem}$ vs $\langle B\rangle_{\rm in}$, both normalized to the corresponding maximum $\langle B\rangle_{\rm rem}$, calculated using both the Bean and simple Kim approximations with no dB/dH effect coming into play and also with discontinuities of various magnitudes introduced in the modeling.

In our view these figures show that the presence or absence of a dB/dH effect will emerge clearly in the $\langle B\rangle_{\rm rem}$ vs $\langle B\rangle_{\rm in}$ format if the dependence of j_c on B is Bean like, but will not stand out unambiguously if the dependence approaches the simple Kim limit.

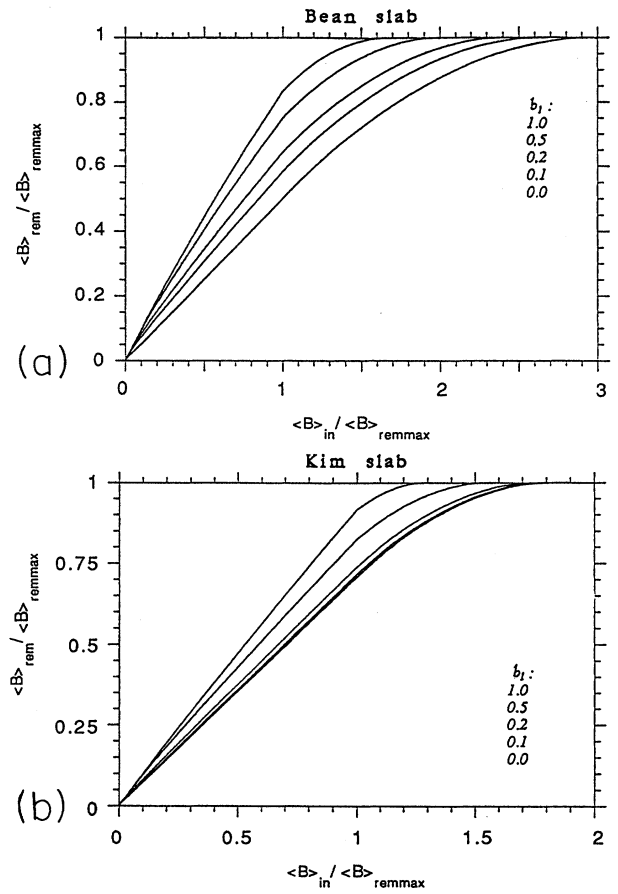

FIG. 8. Displays families of theoretical curves for $\langle B\rangle_{\rm rem}/\langle B\rangle_{\rm rem\,max}$ vs $\langle B\rangle_{\rm in}/\langle B\rangle_{\rm rem\,max}$ calculated for infinite slab geometry using (a) the Bean ($j_c=\alpha$) and (b) the simple Kim ($j_c=\alpha/B$) approximations. $b_1=B^*_{c1}/B_*$ indicates the magnitude of the discontinuity in the B profiles (i.e., the size of the dB/dH effect); hence, $b_1=0$ indicates no discontinuity. The order of the numbers for b_1 corresponds to the order of the curves. $B_*=\mu_0\alpha X$ for the Bean and $B_*=(2\mu_0\alpha X)^{1/2}$ for the Kim case. The expressions for $\langle B\rangle_{\rm rem}$ and $\langle B\rangle_{\rm in}$ are developed in the Appendix. The presence of a discontinuity generates a slope of unity along the initial segment of the curves. The extent of this section increases as b_1 increases.

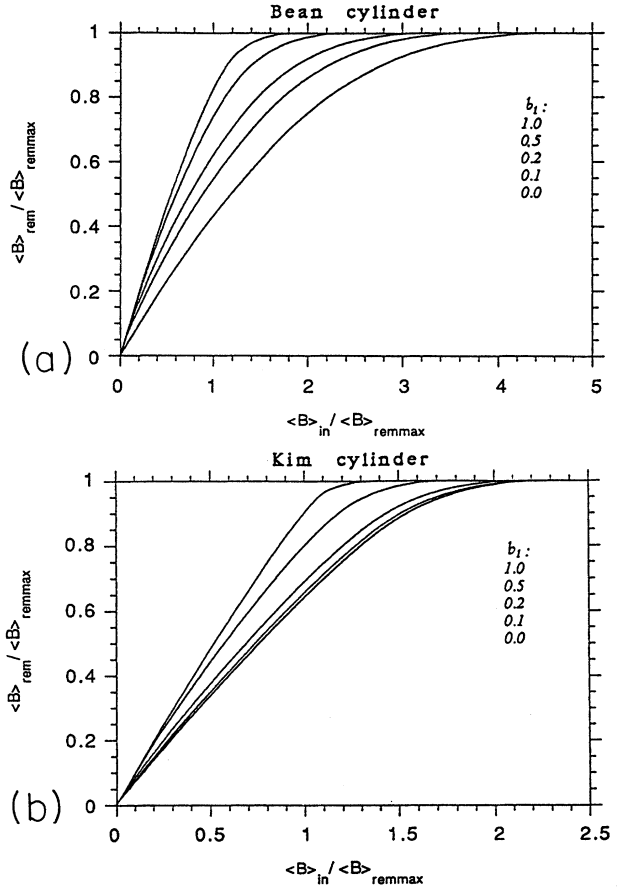

FIG. 9. Same as for Fig. 8 except that here the geometry is that of an infinitely long cylinder and the radius R replaces X in the definition of B_*.

Since the approximation $j_c=\alpha/B$ generates steep gradients in the magnetic-flux density when B is small, and hence already "mimics" a dB/dH effect, it is not surprising that the introduction of a discontinuity in the B profiles causes no dramatic changes in the $\langle B\rangle_{\rm rem}$ vs $\langle B\rangle_{\rm in}$ curves in this case. By contrast and as expected, the introduction of a discontinuity when the Bean approximation is used causes an appreciable shift in the $\langle B\rangle_{\rm rem}$ vs $\langle B\rangle_{\rm in}$ curves.

In practice, however, j_c dependences on B which are *intermediate* between $j_c=\alpha/B$ and $j_c=\alpha$, i.e., between the simple Kim and Bean approximations, are usually encountered and these will generate $\langle B\rangle_{\rm rem}$ vs $\langle B\rangle_{\rm in}$ curves which fall between these two limiting cases. Consequently, we have explored other formats for displaying the data which carry the crucial message on the dB/dH effect more clearly regardless of the details of the dependence of j_c on B.

C. Two more transparent formats: $\langle B\rangle_{\rm rem}/\langle B\rangle_{\rm in}$ vs $\langle B\rangle_{\rm in}$ and vs $\langle B\rangle_{\rm rem}$

We now examine the merits of two modifications of the previous format for revealing unambiguously the role of the dB/dH effect. In these new schemes, the ratios $\langle B\rangle_{\rm rem}/\langle B\rangle_{\rm in}\equiv\mu_0\langle M\rangle_{\rm rem}/\langle B\rangle_{\rm in}$ are plotted versus either $\langle B\rangle_{\rm in}$ or vs $\langle B\rangle_{\rm rem}$. These approaches also divorce or decouple the analysis from $H_{\rm cycle}$ and hence also avoid the complications and uncertainties involved in the link between $H_{\rm cycle}$ and the observed $\langle B\rangle_{\rm rem}$ and $\langle B\rangle_{\rm in}$.

The families of theoretical curves displayed in Figs. 10–13 illustrate the effect of a discontinuity in the evolution of $\langle B\rangle_{\rm rem}/\langle B\rangle_{\rm in}$ vs $\langle B\rangle_{\rm in}$ and $\langle B\rangle_{\rm rem}$ for the same two radically different dependences of j_c on B, exploited earlier, namely, the simple Bean and Kim approximations. The signature of the dB/dH effect emerges quite clearly from a cursory inspection of these theoretical predicted curves. All the curves where a dB/dH effect is postulated to exist exhibit a steep rise towards unity in the low range of $\langle B\rangle_{\rm in}$, no matter how small the discontinuity. Careful consideration of the B profiles sketched in Figs. 2(a) and 2(b) indicates that this behavior is to be expected regardless of the dependence of the bulk critical current density j_c on B and of the variation of I_M and $\Delta H_{\rm en}$ with $H_{\rm cycle}$.

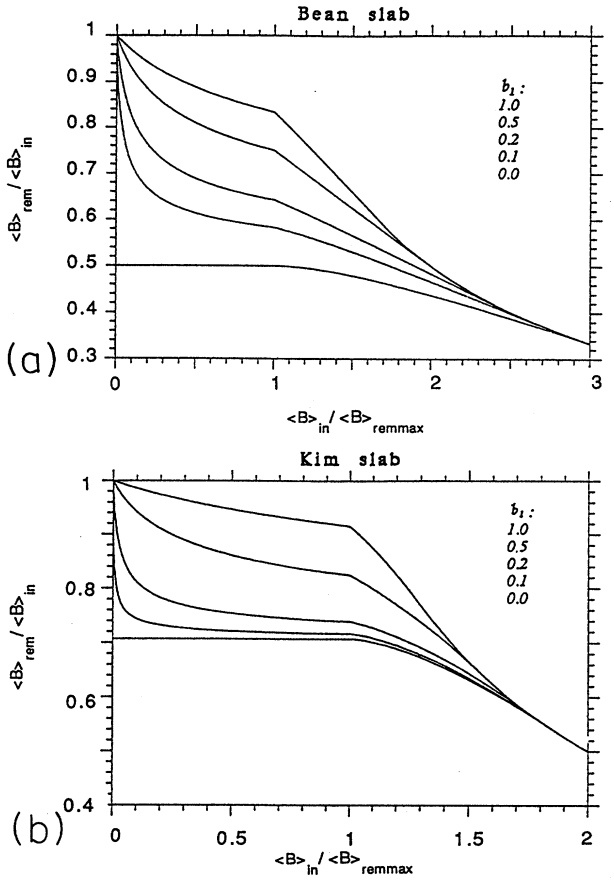

FIG. 10. Displays families of theoretical curves for $\langle B\rangle_{\rm rem}/\langle B\rangle_{\rm in}$ vs $\langle B\rangle_{\rm in}/\langle B\rangle_{\rm rem\,max}$ for infinite slab geometry (see caption to Fig. 8 for other details). The signature of a discontinuity is quite clear in this format since all curves where a discontinuity is present (i.e., $b_1>0$) rise steeply to unity at the origin.

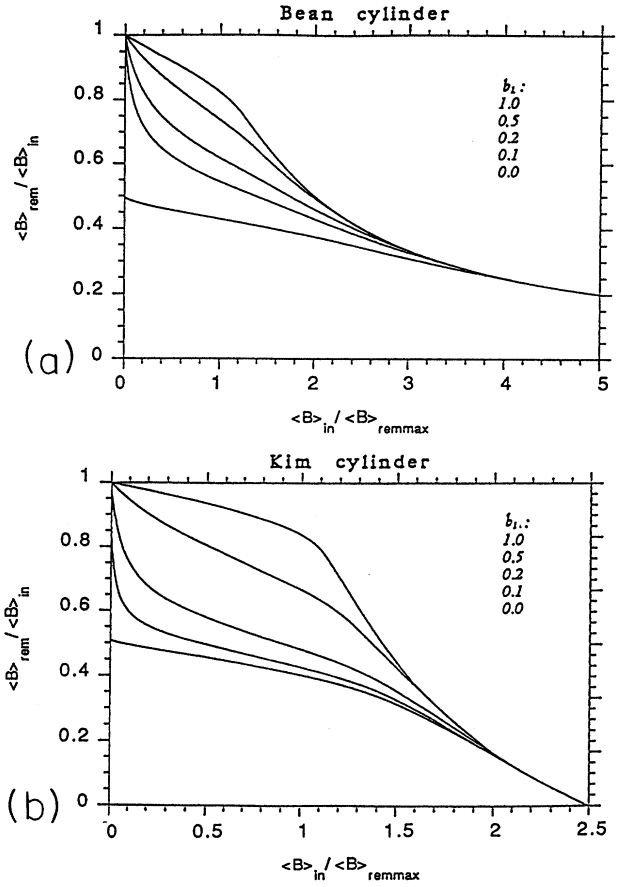

FIG. 11. Same as for Fig. 10 except that here the geometry is that of an infinitely long cylinder.

Figures 14–20 display the data for our five samples in these two equivalent formats. It is clear from inspection that none of the experimental data curves display any hint of a rise toward unity in the initial portions of the curves as required by the operation of a dB/dH effect. Indeed, on the contrary, most of the specimens show a downward trend in this range. We return to this feature later. The vertical spread of the data points at the extreme right of Figs. 16–19 arises because here $\langle B\rangle_{\rm rem}$ has saturated at $\langle B\rangle_{\rm rem\ max}$, but $\langle B\rangle_{\rm in}$ continues to increase.

Between these two formats where the dB/dH effect can emerge clearly, we favor the latter since it has a readily defined limit on the abscissa, whereas for the former the experimental limit where $\langle B\rangle_{\rm in}$ generates $\langle B\rangle_{\rm rem\ max}$ has to be carefully and separately identified from the data curves illustrated in Figs. 1(a) and 1(b). We have therefore displayed only the data for the Nb and PbIn specimens in the former format. These two were selected because they have the largest $B_{c1}/\langle B\rangle_{\rm rem\ max}$ ratios of our samples and illustrate slab and cylinder behavior, respectively.

In each case the display of the data is accompanied by a theoretical (solid) curve. We stress that in each instance the "crude ingredients" of the theoretical curves are identical to the corresponding one presented earlier in Figs. 3–7. Now, however, the fit between the data and the theoretical curves has somewhat deteriorated in most instances. In our view this indicates that the curves of $\langle B\rangle_{\rm rem}/\langle B\rangle_{\rm in}$ vs either $\langle B\rangle_{\rm in}$ or $\langle B\rangle_{\rm rem}$, besides being dramatically affected by the presence of a dB/dH effect, are also more sensitive to the detailed dependence of j_c on B than the standard format and the $\langle B\rangle_{\rm rem}$ vs $\langle B\rangle_{\rm in}$ format. To achieve good agreement between calculations and observations, more sophisticated and complicated expressions for $j_c(B)$ are evidently needed now than were required by the other less discriminating formats. The simple approximate analytic functions exploited in our analysis now appear inadequate. The central purpose of our investigation, however, was not to identify the optimum expressions for j_c as a function of B for our samples, but to establish whether the stipulation of a dB/dH effect is corroborated by the data.

It is instructive, however, to dwell briefly on one feature of some of the data. The PbBi, Nb, and NbTa specimens display a weak convex upward curvature. In our view this behavior arises from the fact that in these specimens the dependence of j_c on B is intermediate between the simple Kim and Bean approximations. Theoretical curves incorporating no dB/dH effect and calculated using $j_c=\alpha/(B+B_0)$ with different values for B_0 are displayed in

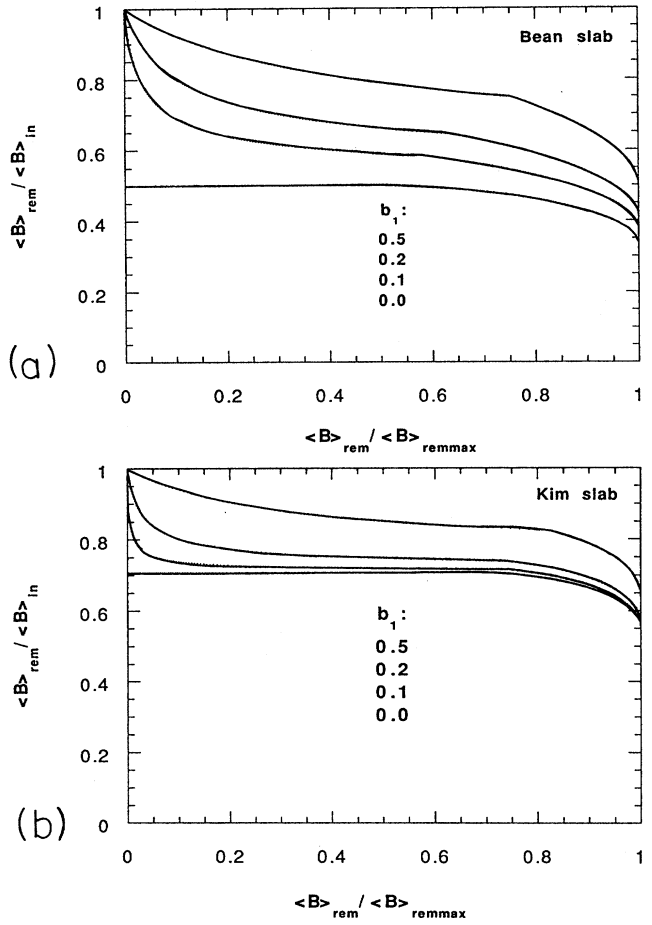

FIG. 12. Displays families of theoretical curves for $\langle B\rangle_{\rm rem}/\langle B\rangle_{\rm in}$ vs $\langle B\rangle_{\rm rem}/\langle B\rangle_{\rm rem\,max}$ for infinite slab geometry (see caption to Fig. 8 for other details). The signature of a discontinuity is even more dramatically clear in this alternative format since all curves where a discontinuity is present (i.e., $b_1>0$) not only rise steeply to unity at the origin, but the range where the rise occurs is now "expanded."

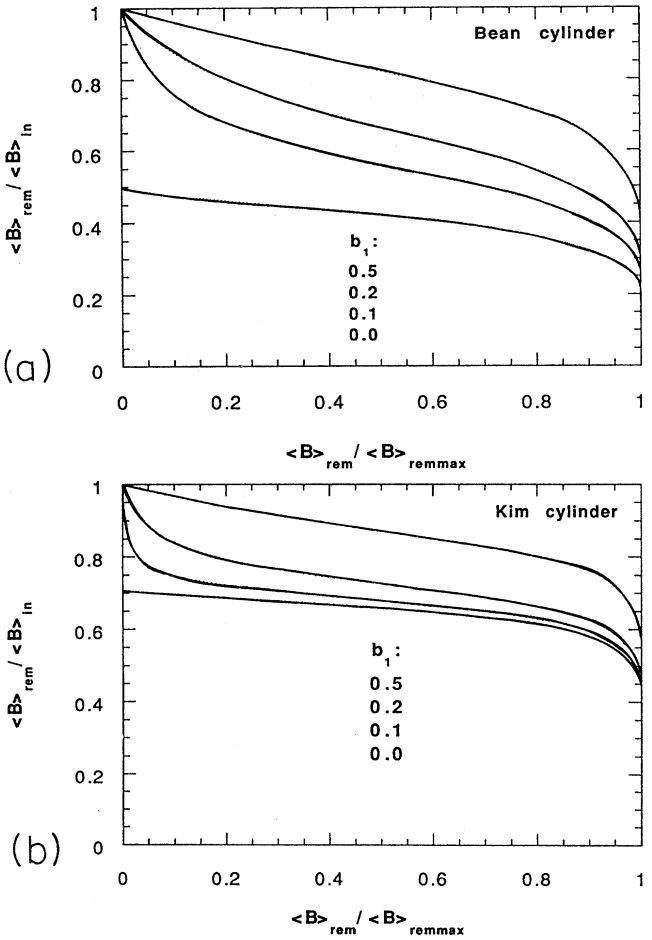

FIG. 13. Same as for Fig. 12 except that here the geometry is that of an infinitely long cylinder.

Fig. 21 for idealized slab and cylinder geometry. We note that these theoretical curves exhibit a hump or peak qualitatively similar to that encountered in some of our data curves.

D. Completely asymmetric *dB/dH* effect

In the foregoing we have focused on remanent flux configurations where the *dB/dH* effect (discontinuity in the *B* profile) was visualized to occur in any region where the magnetic-flux density of the *B* profile fell below a critical threshold B_{c1}^*. Thus we envisaged "symmetric" remanent *B* profiles after an excursion of the surface flux density B_S in the range $B_{c1}^*<B_S\leq B_S^*$[see Fig. 2(e)] and always postulated a discontinuity of magnitude B_{c1}^* at the surface of the specimen in our modeling of the remanent *B* profiles [see Figs. 2(e)–2(h)]. Several workers, however, have reported evidence that the image force attraction in weak-pinning materials may lead to a continuous magnetic-flux density across the surface on a quasimacroscopic scale as the externally applied magnetic field is reduced from $H_{\rm cycle}>H_{c1}+\Delta H_{\rm en}$ to zero.[1,13,37–43] Consequently, we need to consider the possibility that the *dB/dH* effect could be suppressed by this or other mechanisms at the surface of the specimen in the remanent trapped flux state while yet occurring in the *B* profile far from the surface.

Sequences of *B* profiles envisaged to occur when no discontinuity exists (no *dB/dH* effect operates), hence $B_{\rm ex}=0$, at the surface of the specimen are sketched in Fig. 22. The expressions for the corresponding $\langle B\rangle_{\rm rem}=\mu_0\langle M\rangle_{\rm rem}$ vs B_S are developed in the Appendix exploiting the prescription that $j_c=\alpha/(B_0+B)^n$. Graphs of families of $\langle B\rangle_{\rm rem}/\langle B\rangle_{\rm in}$ vs $\langle B\rangle_{\rm rem}/\langle B\rangle_{\rm rem\ max}$, where $B_{\rm ex}=0$ and $b_1=B_{c1}^*/B_*$ is varied from 0 to 1, are presented in Figs. 23 and 24 for ideal slab and cylinder geometry for the Bean ($n=0$) and simple Kim ($n=1, B_0=0$) cases. The crucial feature which emerges from this analysis is that now $\langle B\rangle_{\rm rem}/\langle B\rangle_{\rm in}$ descends to zero as $\langle B\rangle_{\rm rem}$ becomes vanishingly small if a *dB/dH* effect (i.e., $b_1>0$) is postulated during the flux penetration. A comparison of these theoretical curves with our data displayed in the same format (see Figs. 16–20) shows that the behavior predicted by a completely asymmetric *dB/dH* effect regime

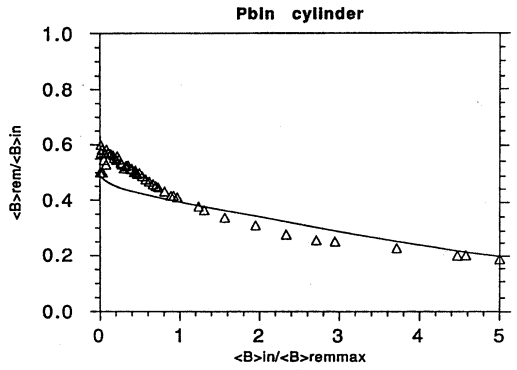

FIG. 14. Display of our data for the PbIn cylinders (wires) in the $\langle B\rangle_{\rm rem}/\langle B\rangle_{\rm in}$ vs $\langle B\rangle_{\rm in}/\langle B\rangle_{\rm rem\,max}$ format. It is evident that the data do not rise toward unity near the origin. The solid curve is theoretical and calculated using the same input as that for Fig. 3 where no discontinuity was introduced.

(i.e., where $b_1>0$ inside and $B_{\rm ex}=0$ at the surface) is not supported by our observations.

V. SUMMARY AND CONCLUSION

The remanent magnetic-flux density $\langle B\rangle_{\rm rem}=\mu_0\langle M\rangle_{\rm rem}$ trapped in type-II superconductors is frequently measured and plotted vs $H_{\rm cycle}$, the magnetic field whose application to the zero-field-cooled specimen and subsequent removal generated the residual magnetization $\langle M\rangle_{\rm rem}$. The modeling of these data curves requires information on (i) the variation of the magnitude of the Meissner shielding current I_M and the barrier to flux entry $\Delta H_{\rm en}$ as a function of $H_{\rm cycle}$ and (ii) the magnitude of the discontinuity in the B profile (dB/dH effect) in the interior and at the surface of the specimen. Analysis of measurements of $\langle B\rangle_{\rm in}$, the magnetic-flux density permeating the specimen vs $H_{\rm cycle}$, also confronts the same problems. The parametric relationship between $\langle B\rangle_{\rm rem}$ and $\langle B\rangle_{\rm in}$ via B_S, the magnetic-flux density just inside the surface, avoids the need to determine I_M and $\Delta H_{\rm en}$ in the search for evidence of a dB/dH effect in the configuration of the magnetic-flux density.

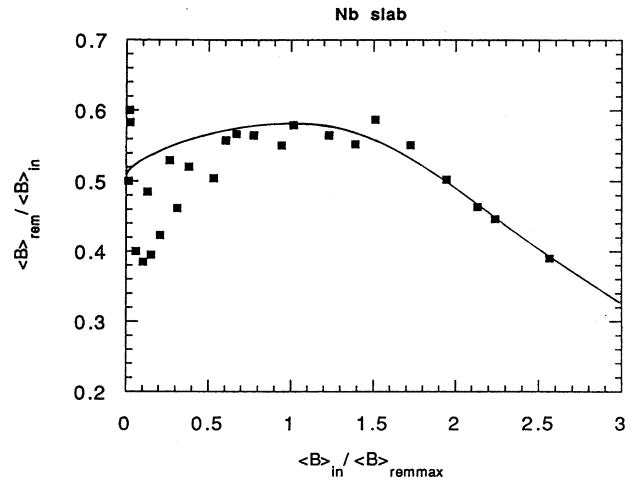

FIG. 15. Display of our data for the Nb ribbons in the $\langle B\rangle_{\rm rem}/\langle B\rangle_{\rm in}$ vs $\langle B\rangle_{\rm in}/\langle B\rangle_{\rm rem\,max}$ format. It is evident that the data lie far below unity near the origin. The solid curve is theoretical and calculated using the same input as that for Fig. 5 where no discontinuity was introduced.

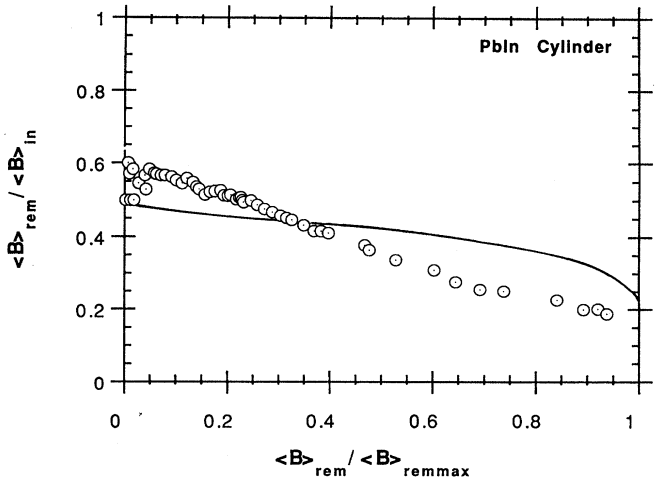

FIG. 16. Display of our data for the PbIn sample in the $B_{\rm rem}/\langle B\rangle_{\rm in}$ vs $\langle B\rangle_{\rm rem}/\langle B\rangle_{\rm rem\,max}$ format. See caption to Figs. 14 and 3 for calculated solid curves.

We have shown that plots of the ratio $\langle B\rangle_{\rm rem}/\langle B\rangle_{\rm in}$ vs either $\langle B\rangle_{\rm in}$ or $\langle B\rangle_{\rm rem}$ are particularly sensitive to the presence of a "discontinuity" in the B profiles associated with the dB/dH effect. We have pursued in detail two scenarios encountered in the literature.[1–12,38–43] In one scenario, the dB/dH effect leads to a discontinuity at the front of the penetrating flux-density profile (B^*_{c1}) and a discontinuity of equal magnitude ($B_{\rm ex}=B^*_{c1}$) at the surface after H_a has been removed. This is labeled the symmetric dB/dH effect. In the second scenario, no discontinuity exists at the surface in the

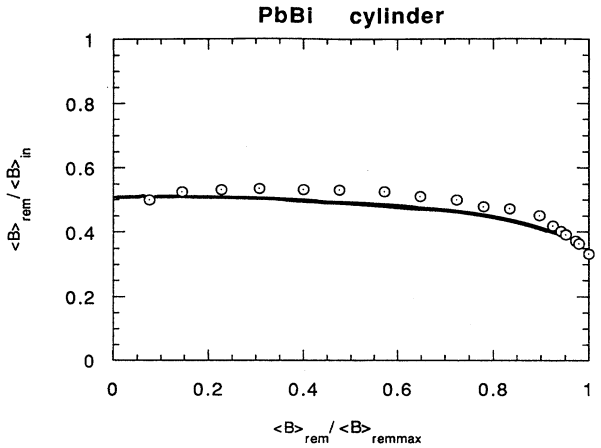

FIG. 17. Display of our data for the PbBi sample in the $\langle B\rangle_{\rm rem}/\langle B\rangle_{\rm in}$ vs $\langle B\rangle_{\rm rem}/\langle B\rangle_{\rm rem\,max}$ format. The solid curve is theoretical and calculated using the same input as that for Fig. 4 where no discontinuity was introduced.

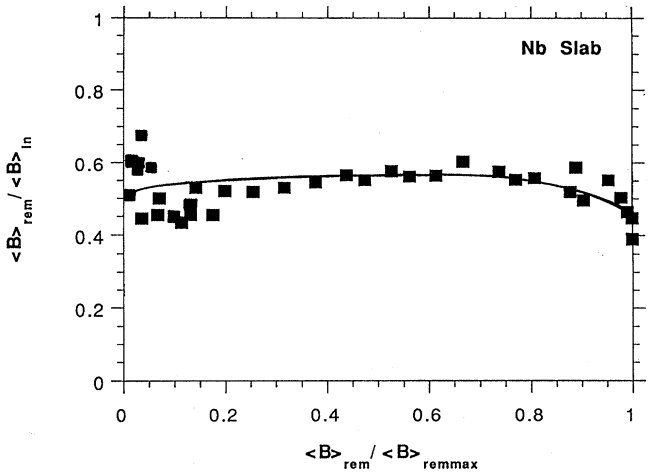

FIG. 18. Display of our data for the Nb ribbons in the $\langle B\rangle_{\rm rem}/\langle B\rangle_{\rm in}$ vs $\langle B\rangle_{\rm rem}/\langle B\rangle_{\rm rem\,max}$ format. See caption to Figs. 15 and 5 for theoretical solid curves.

remanent flux-density profile ($B_{\rm ex}=0$), but $B_{c1}^{*}>0$ in the penetrating B profile. This is denoted the completely asymmetric dB/dH effect. For both frameworks we have calculated families of curves for a wide range of B_{c1}^{*}. The formulas we develop and present in the Appendix encompass a broad scenario where $0\leq B_{\rm ex}\leq B_{c1}^{*}$. Theoretical results were obtained for idealized slab and cylinder geometry and dependences of the bulk critical current density j_c on B of the general form $j_c=\alpha/(B+B_0)^n$. The crucial features which emerge from the theoretical analysis is that the presence of a dB/dH effect, however minute, dictates in these two discriminating formats, regardless of the details of the dependence of j_c on B, (i) an initial rise toward unity in the first scenario and (ii) an initial descent toward zero in the second scenario. A comparison of our data for five different materials with predictions provides no support for the existence or a symmetric or completely asymmetric dB/dH effect.

The Nb and PbIn data are most cogent since here $B_{c1}\approx\langle B\rangle_{\rm rem\,max}$. This indicates that, in the saturated remanent state, the bulk critical current filling the entire specimen

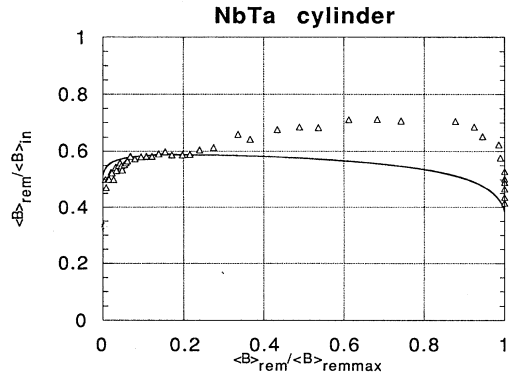

FIG. 19. Display of our data for the NbTa sample in the $\langle B\rangle_{\rm rem}/\langle B\rangle_{\rm in}$ vs $\langle B\rangle_{\rm rem}/\langle B\rangle_{\rm rem\,max}$ format. The solid curve is theoretical and calculated using the same input as for Fig. 6.

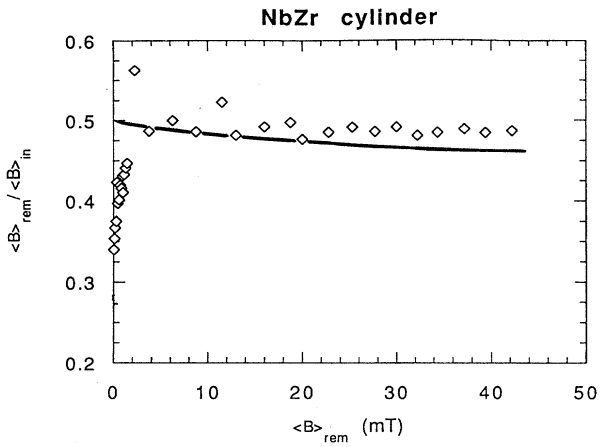

FIG. 20. Display of our data for the NbZr sample in the $\langle B\rangle_{\rm rem}\langle B\rangle_{\rm in}$ vs $\langle B\rangle_{\rm rem}$ format. The solid curve is theoretical and calculated using the same input as for Fig. 7.

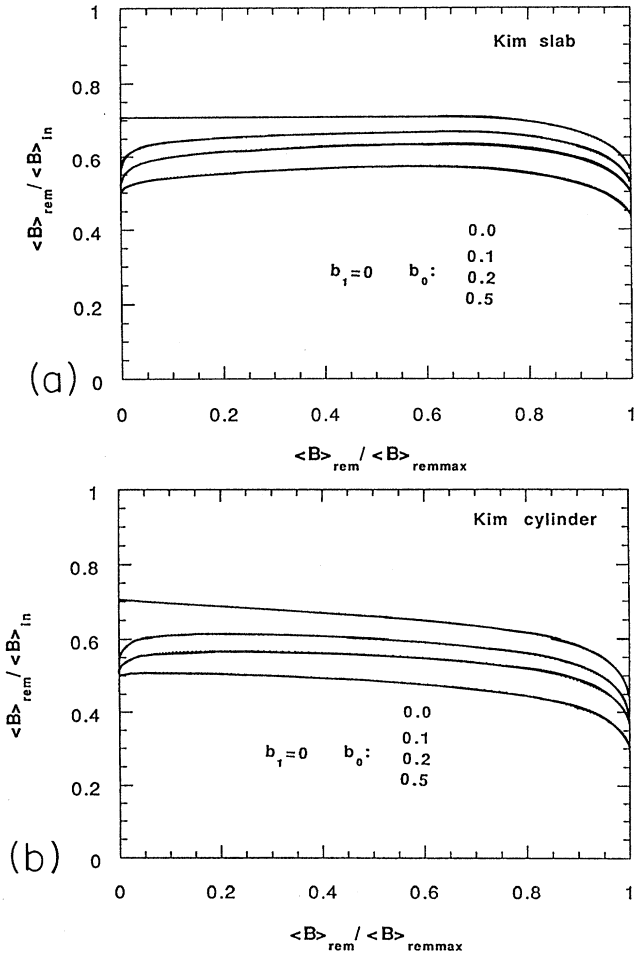

FIG. 21. Display of the effect of the parameter $b_0=B_0/B_*$ on the evolution of $\langle B\rangle_{\rm rem}/\langle B\rangle_{\rm in}$ vs $\langle B\rangle_{\rm rem}/\langle B\rangle_{\rm rem\,max}$ curves for ideal slab and cylinder geometry when $b_1=0$, hence when no discontinuities are present in the B profiles. Here $j_c=\alpha/(B+B_0)^n$ and $n=1$ (Kim case). The formulas are developed in the Appendix.

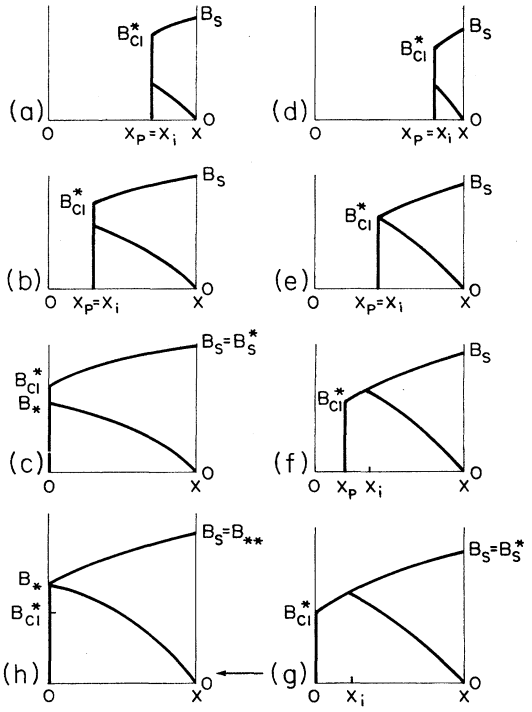

FIG. 22. Schematics of the B profiles vs increasing B_S for the case where a discontinuity (dB/dH effect) of magnitude B_{c1}^* exists during flux penetration (upper curves in each sketch), but no discontinuity (no dB/dH effect) occurs at the surface when $H_{\rm cycle}$ has been removed (lower curves in each sketch). Two situations need to be considered. (i) $B_{c1}^*>B_*$ in (a)–(c) and (ii) $B_{c1}^*<B_*$ for (d)–(h). Expressions for $\langle B\rangle_{\rm rem}$ vs B_S for this "completely asymmetric" dB/dH effect regime are developed in the Appendix.

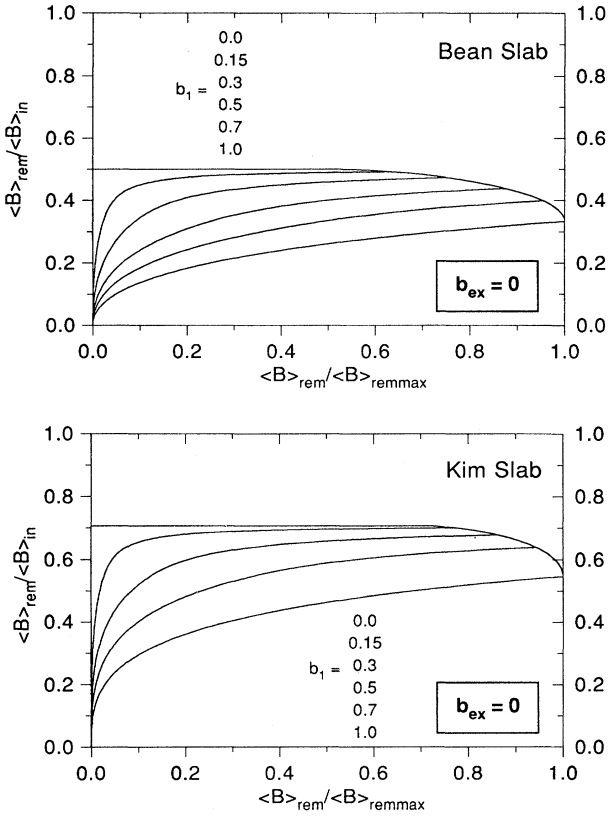

FIG. 23. Displays families of theoretical curves for $\langle B\rangle_{\rm rem}/\langle B\rangle_{\rm rem\,max}$ vs $\langle B\rangle_{\rm in}/\langle B\rangle_{\rm rem\,max}$ for the completely asymmetric regime calculated for slab geometry using the Bean ($j_c=\alpha$) and simple Kim ($j_c=\alpha/B$) approximation; $b_1=B_{c1}^*/B_*$ denotes the discontinuity in the B profile occurring during flux penetration. However, no discontinuity (no dB/dH effect) exists at the surface after removal of $H_{\rm cycle}$. The latter feature is denoted by $B_{\rm ex}=0$.

of dimension X or $R\approx 100\lambda$ generates, by Ampère's law, a maximum field at the center, $H_{\rm cen}\approx\int_0^X j_c dx=\int_0^R j_c dr$, comparable to H_{c1}. In these two samples any abrupt spatial variation of the magnetic-flux density comparable to $\mu_0 H_{c1}$ over a dimension $\approx\lambda\approx X/100$ or $R/100$ (i.e., a dB/dH effect) would be a very salient feature and emerge quite clearly in the two discriminating formats we have proposed.

The structure of the advancing flux front in thin films and single crystals of high-T_c and conventional type-II superconductors when a magnetic field piercing the broad surfaces of the specimens is impressed has been investigated recently exploiting high-resolution magneto-optical techniques. Indenbom *et al.*[47] report the observation of a flux step $\sim B_{c1}$ between regions of magnetic flux of opposite polarities in the remanent state of Bi 2212 single crystals of typical dimensions $1.2\times 2.5\times 0.04$ mm^3. These workers find that the optimal conditions for the observations of flux steps are fulfilled in a temperature range where j_c has decreased to $j_c=H_{c1}/d$, where d is the thickness of the specimen. Durán *et al.*[48] observe that the critical state picture of uniform flux fronts breaks down at temperatures far below T_c in thin films of niobium and that the penetration of the field takes place through the growth of magnetic dendrites. They also find that the dendrites can grow by nucleating large regions of antivortices. The application of these sensitive techniques to the study of the flux front piercing the flat ends of long cylinders or the top surface of a stack of single crystals of identical contours should shed further light on the role of finite geometries (return fields) on these phenomena and on the dB/dH effect.

APPENDIX

In this appendix we develop explicit expressions for $\langle B\rangle_{\rm in}$ and $\langle B\rangle_{\rm rem}$ for a wide variety of remanent trapped flux configurations for idealized planar and cylinder geometry exploiting the frequently used prescription for the critical current density j_c,

$$j_c=\frac{\alpha}{(B+B_0)^n}, \tag{A1}$$

where α and B_0 are temperature-dependent parameters characterizing the specimen.

We consider (a) a slab infinite along the y and z axis of thickness $a=2X$ with surfaces located at $x=\pm X$ and (b) an infinitely long cylinder of radius R centered on the z axis.

Maxwell's equation $\nabla\times\vec{B}=\mu_0\vec{j}$ for our idealized geometries, together with the critical state assumption that wher-

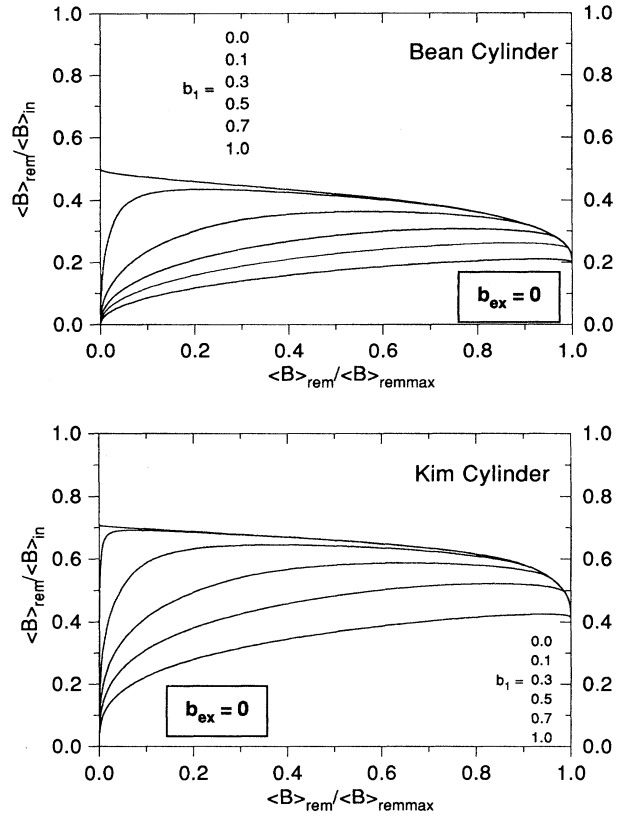

FIG. 24. Same as for Fig. 23 except that here the geometry is that of an infinitely long cylinder.

ever changes of magnetic-flux density have occurred, the induced current exists in a critical state, leads to

$$\frac{dB}{dx}=\pm\frac{\mu_0\alpha}{(B_0+B)^n}=\frac{dB}{dr}. \tag{A2}$$

Integrating from x to X or from r to R in the volume where $j\neq 0$ (see Fig. 25), Eq. (A2) reads

$$\int_x^X (B_0+B)^n d(B_0+B)=\pm\mu_0\alpha\int_x^X dx, \tag{A3a}$$

$$\int_r^R (B_0+B)^n d(B_0+B)=\pm\mu_0\alpha\int_r^R dr. \tag{A3b}$$

Faraday's law of magnetic induction and previous history in the superconducting state determine the sign of j. We let B_s denote the magnetic-flux density just inside the specimen a distance of the order of λ from the surface. Thus the expressions for $B(x)$ and $B(r)$ (i.e., the B profiles) will depend explicitly on B_s, but will be "decoupled" from H_a although B_s is linked to $H_a=H_{\rm cycle}$ by $B_s/\mu_0=H_{\rm cycle}-I_M-\Delta H_{\rm en}$ [Eq. (6) of the main text].

We let B_{c1}^* denote the magnitude of the "discontinuity" in the B profiles (the dB/dH effect) as the flux front penetrates into the specimen. For generality, we also postulate a discontinuity $B_{\rm ex}\leq B_{c1}^*$ at the surface in the remanent trapped flux profile. The families of calculated curves presented in this

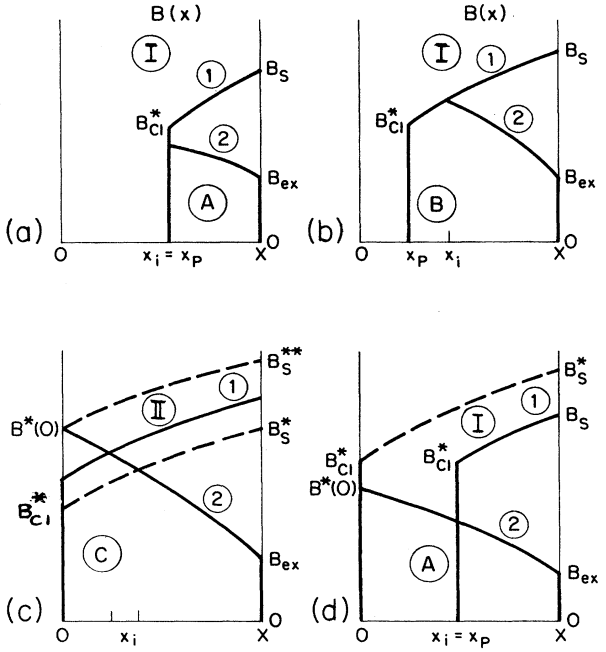

FIG. 25. Schematics of the evolution of the B profiles (i) when B_S, the magnetic-flux density just inside the surface, is increased above B_{c1}^*, the magnitude of the discontinuity (dB/dH effect) at the front of the penetrating flux density profile, and (ii) after the corresponding applied field $H_{\rm cycle}$ (not shown) has been reduced to zero. Two regimes of flux penetration need to be envisaged. In regime I, x_p or r_p, the front of the B profile lies in the range $0<x_p<X$ or $0<r_p<R$. In regime II, $B(0)$, the magnetic-flux density at the midplane (axis) of the specimen rises from B_{c1}^* to $B^*(0)=[\{(B_{\rm ex}+B_0)^{n+1}+B_*\}^{1/(n+1)}-B_0]$ as B_S increases from B_S^* to B_S^{**}. For generality we have displayed and developed expressions for the remanent B profiles where B_{c1}^*, the discontinuity inside the specimen, may be different from and larger than $B_{\rm ex}$, the resultant discontinuity (dB/dH effect diminished by the action of the image force attraction) at the surface. Two cases must be considered in the evolution of the remanent B profiles; namely, $B_{c1}^*<B^*(0)$ displayed in (a)–(c) and $B_{c1}^*>B^*(0)$ displayed in (d). For the first case, a sequence of three regimes must be taken into account. For regime A, $x_i=x_p\neq 0$ as displayed in (a). For regime B, $x_i>x_p\neq 0$ as displayed in (b). For regime C, $x_i\neq 0$, $x_p=0$ as displayed in (c). For the second case, only regime A where $x_i=x_p\neq 0$ is encountered as displayed in (d).

article focus on (i) the "symmetric" dB/dH effect scenario where $B_{\rm ex}=B_{c1}^*\neq 0$ and (ii) the completely asymmetric situation where $B_{\rm ex}=0$ and $B_{c1}^*>0$. However, the expressions we develop for $\langle B\rangle_{\rm rem}$ in this appendix encompass a spectrum of configurations where $0\leq B_{\rm ex}\leq B_{c1}^*$ and $B_{c1}^*\leq B_*$, where B_* is defined below. We refer the reader to Fig. 25 for a display of the various symbols. Regimes I and II are encountered for the initial entering flux configurations where $H_a=H_{\rm cycle}$ and regimes A, B, and C encompass the variety of remanent flux profiles after H_a has been removed.

To avoid repetition we now focus on Eq. (A3b) noting that substituting x for r and X for R in the formulas below describes the B profiles for the right half of an infinite slab whose midplane is situated at $x=0$ and its surface at $x=\pm X$. We let $B_1(r)$ denote the initial profile when $\mu_0 H_a$ is

present and $B_2(r)$ the remanent profile in the volume where some flux was released during the removal of H_a.

Integrating Eq. (A3b) leads to

$$(B_0+B_s)^{n+1}-[B_0+B_1(r)]^{n+1}=B_*^{n+1}\left(1-\frac{r}{R}\right) \quad \text{(A4)}$$

for the $B_1(r)$ profiles (positive slope) and

$$(B_0+B_{ex})^{n+1}-[B_0+B_2(r)]^{n+1}=-B_*^{n+1}\left(1-\frac{r}{R}\right) \quad \text{(A5)}$$

for the $B_2(r)$ profiles (negative slope).

Here for convenience we have written

$$B_*^{n+1}=(n+1)\mu_0\alpha R. \quad \text{(A6)}$$

We note that B_* corresponds to the first full penetration field for the case where $B_0=0$ and $B_{c1}^*=0$.

r_p, the position of the front of the advancing B profile, is obtained from Eq. (A4) since, here,

$$B_1(r)=B_1(r_p)=B_{c1}^*. \quad \text{(A7)}$$

This leads to

$$B_*^{n+1}\left(1-\frac{r_p}{R}\right)=(B_0+B_s)^{n+1}-(B_0+B_{c1}^*)^{n+1}, \quad \text{(A8)}$$

which is valid until r_p advances to the center and B_s attains the full penetration value B_s^* where

$$B_s^*=[(B_0+B_{c1}^*)^{n+1}+B_*^{n+1}]^{1/(n+1)}-B_0, \quad \text{(A9)}$$

which is obtained by letting $r_p=0$ in Eq. (A8). This is the first full penetration field if $B_0\neq 0$ and $B_{c1}^*\neq 0$.

Regime I for the flux penetration applies over the range

$$B_{c1}^*<B_s\leq B_s^*. \quad \text{(A10)}$$

In regimes B and C for $\langle B\rangle_{rem}$ (see Fig. 25), $B_2(r)$, the remanent B profile, intersects $B_1(r)$, the initial profile. The position of the intersection of the $B_1(r)$ and $B_2(r)$ profiles is obtained by letting $r=r_i$ in Eqs. (A4) and (A5) and noting that

$$B_1(r_i)=B_2(r_i). \quad \text{(A11)}$$

Introducing Eqs. (A4) and (A5) into (A11) and solving for r_i leads to

$$B_*^{n+1}\left(1-\frac{r_i}{R}\right)=\frac{(B_0+B_s)^{n+1}-(B_0+B_{ex}^*)^{n+1}}{2}. \quad \text{(A12)}$$

Equation (A12) is valid until $r_i=0$ and B_s attains a value B_s^{**} where,

$$B_s^{**}=[(B_0+B_{ex})^{n+1}+2B_*^{n+1}]^{1/(n+1)}-B_0, \quad \text{(A13)}$$

which is obtained by letting $r_i=0$ in Eq. (A12). Equation (A13) dictates the upper limit of regime C and Eq. (A9) its lower limit. For this regime, $r_p=0$ and $0\leq r_i$.

For regime B, $r_p\neq 0$ and $r_i>r_p$. This regime commences when $r_i=r_p$ and

$$B_1(r_p)=B_2(r_i)=B_{c1}^*. \quad \text{(A14)}$$

Hence introducing (A14) into (A4) and (A5), we find the lower limit for regime B to read

$$B_s=[2(B_0+B_{c1}^*)^{n+1}-(B_0+B_{ex})^{n+1}]^{1/(n+1)}-B_0. \quad \text{(A15)}$$

For regime A, $r_i=r_p>0$ and

$$B_2(r_i)<B_1(r_p)=B_{c1}^*. \quad \text{(A16)}$$

This regime commences when $B_s>B_{c1}^*$ and terminates when regime B commences.

We note, however, that, as illustrated in Fig. 25(d), regime A is the only remanent flux density profile regime which is encountered if

$$B^*(0)=B_2(0)=[\{(B_0+B_{ex})^{n+1}+B_*^{n+1}\}^{1/(n+1)}-B_0] \leq B_{c1}^*. \quad \text{(A17)}$$

$\langle B\rangle_{in}$, the spatial average of the magnetic flux permeating the sample when $\mu_0 H_a$ is present, is obtained by introducing Eq. (A4) in the form

$$B_1(x)=B_1(r)=\left[(B_0+B_s)^{n+1}-B_*^{n+1}\left(1-\frac{r}{R}\right)\right]^{1/(n+1)}-B_0 \quad \text{(A18)}$$

in the definition

$$\langle B\rangle_{in}=\frac{1}{X}\int_{x_p}^{X}B_1(x)dx \quad \text{(A19)}$$

and

$$\langle B\rangle_{in}=\frac{2}{R^2}\int_{r_p}^{R}B_1(r)r\,dr. \quad \text{(A20)}$$

We note that for regime II, $x_p=0$, $r_p=0$. Regime II has no upper limit since the upper critical field B_{c2} is not taken into account in Eq. (A1). In our analysis, when $B^*(0)>B_{c1}^*$, the pertinent range of regime II extends from B_s^* to B_s^{**}, the upper limit of regime C [see Fig. 25(c)]. Regime II does not come into play when $B^*(0)\leq B_{c1}^*$ [see Fig. 25(d)].

$\langle B\rangle_{rem}$, the spatial average of the magnetic flux threading the specimen after H_a has been removed, is obtained by introducing Eqs. (A18) and (A5) in the form

$$B_2(x)=B_2(r)=\left[(B_0+B_{ex}^*)^{n+1}+B_*^{n+1}\left(1-\frac{r}{R}\right)\right]^{1/(n+1)}-B_0 \quad \text{(A21)}$$

in the definitions

$$\langle B\rangle_{rem}=\frac{1}{X}\int_{x_p}^{x_i}B_1(x)dx+\frac{1}{X}\int_{x_i}^{X}B_2(x)dx \quad \text{(A22)}$$

and

$$\langle B\rangle_{rem}=\frac{2}{R^2}\int_{r_p}^{r_i}B_1(r)r\,dr+\frac{2}{R^2}\int_{r_i}^{R}B_2(r)r\,dr. \quad \text{(A23)}$$

Again, we note that, for regime C, $x_p=0$, $r_p=0$.

Bearing in mind the limits of integration [Eqs. (A8) and (12)], that regime I corresponds to the range $B_{c1}^{*}<B_s\leq B^{*}$ [given by Eq. (A9)] and regime II to the range $B_s^{*}\leq B_s\leq B_s^{**}$ [given by Eq. (A13)], the pertinent definitions together with the expressions for the B_1 and B_2 profiles [Eqs. (A18) and (A21)] lead to the following formulas where, for brevity, we have introduced normalized quantities which we now define:

$$b_0\equiv\frac{B_0}{B_*},\quad b_1\equiv\frac{B_{c1}^{*}}{B_*},\quad b_{\rm ex}=\frac{B_{\rm ex}}{B_*},\tag{A24}$$

$$b_s\equiv\frac{B_s}{B_*},\quad B_*^{n+1}=(n+1)\mu_0\alpha R=(n+1)\mu_0\alpha X.$$

1. Slab geometry

Regime I:

$$\frac{\langle B\rangle_{\rm in}}{B_*}=\left(\frac{n+1}{n+2}\right)\{(b_0+b_s)^{n+1}-(b_0+b_1)^{n+1}\}-b_0\{(b_0+b_s)^{n+1}-(b_0+b_1)^{n+1}\}\tag{A25}$$

valid for $b_1\leq b_s\leq b_s^{*}=[\{(b_0+b_1)^{n+1}+1\}^{1/(n+1)}-b_0]$.

Regime II:

$$\frac{\langle B\rangle_{\rm in}}{B_*}=\left(\frac{n+1}{n+2}\right)[(b_0+b_s)^{n+1}-\{(b_0+b_s)^{n+1}-1\}^{(n+2)/(n+1)}]-b_0\tag{A26}$$

valid for $b_s\geq b_s^{*}$.

Regime A:

$$\frac{\langle B\rangle_{\rm rem}}{B_*}=\left(\frac{n+1}{n+2}\right)[\{(b_0+b_{\rm ex})^{n+1}+(b_0+b_s)^{n+1}-(b_0+b_1)^{n+1}\}^{(n+2)/(n+1}-\{b_{\rm ex}+b_0\}^{n+2}]$$
$$-b_0\{(b_0+b_s)^{n+1}-(b_0+b_1)^{n+1}\}\tag{A27}$$

valid for $b_1<b_s\leq[\{2(b_0+b_1)^{n+1}-(b_0+b_{\rm ex})^{n+1}\}^{1/(n+1)}-b_0]$ if $b^{*}(0)=[\{b_0+b_{\rm ex})^{n+1}+1\}^{1/(n+1)}-b_0]\geq b_1$ [see Figs. 25(a) and 25(b)]. Regime A terminates when $b_s=b_s^{*}=[\{(b_0+b_1)^{n+1}+1\}^{1/(n+1)}-b_0]$ if $b^{*}(0)<b_1$. In this case regimes B and C are not encountered [see Fig. 25(d)].

Regime B:

$$\frac{\langle B\rangle_{\rm rem}}{B_*}=\left(\frac{n+1}{n+2}\right)\left[2\left\{\frac{(b_0+b_s)^{n+1}+(b_0+b_{\rm ex})^{n+1}}{2}\right\}^{(n+2)/(n+1)}-(b_0+b_1)^{n+2}-(b_0+b_{\rm ex})^{n+2}\right]$$
$$-b_0\{(b_0+b_s)^{n+1}-(b_0+b_1)^{n+1}\}\tag{A28}$$

valid for $\{2(b_0+b_1)^{n+1}-(b_0+b_{\rm ex})^{n+1}\}\leq(b_0+b_s)^{n+1}\leq\{(b_0+b_1)^{n+1}+1\}$.

Regime C:

$$\frac{\langle B\rangle_{\rm rem}}{B_*}=\left(\frac{n+1}{n+2}\right)\left[2\left\{\frac{(b_0+b_s)^{n+1}+(b_0+b_{\rm ex})^{n+1}}{2}\right\}^{(n+2)/(n+1)}-(b_0+b_{\rm ex})^{n+2}-\{(b_0+b_s)^{n+1}-1\}^{(n+2)/(n+1)}\right]-b_0\tag{A29}$$

valid for $\{(b_0+b_1)^{n+1}+1\}\leq(b_0+b_s)^{n+1}\leq\{(b_0+b_{\rm ex})^{n+1}+2\}$.

$$\frac{\langle B\rangle_{\rm rem\,max}}{B_*}=\left(\frac{n+1}{n+2}\right)[\{(b_0+b_{\rm ex})^{n+1}+1\}^{(n+2)/(n+1)}-(b_0+b_{\rm ex})^{n+2}]-b_0.\tag{A30}$$

2. Cylindrical geometry

The ranges of validity of the various expressions for cylindrical geometry are identical to that for the corresponding regimes in slab geometry.

Regime I:

$$\frac{\langle B\rangle_{\rm in}}{B_*}=\frac{2(n+1)}{(2n+3)}\{(b_0+b_s)^{2n+3}-(b_0+b_1)^{2n+3}\}+\frac{2(n+1)}{(n+2)}\{(b_0+b_s)^{n+1}-1\}\{(b_0+b_1)^{n+2}-(b_0+b_s)^{n+2}\}$$
$$-b_0\{(b_0+b_s)^{n+1}-(b_0+b_1)^{n+1}\}\{2+(b_0+b_1)^{n+1}-(b_0+b_s)^{n+1}\}. \tag{A31}$$

Regime II:

$$\frac{\langle B\rangle_{\rm in}}{B_*}=\frac{2(n+1)}{(2n+3)}[(b_0+b_s)^{2n+3}-\{(b_0+b_s)^{n+1}-1\}^{(2n+3)/(n+1)}]$$
$$+\frac{2(n+1)}{(n+2)}\{(b_0+b_s)^{n+1}-1\}[\{(b_0+b_s)^{n+1}-1\}^{(n+2)/(n+1)}-(b_0+b_s)^{n+2}]-b_0. \tag{A32}$$

Regime A:

$$\frac{\langle B\rangle_{\rm rem}}{B_*}=\frac{2(n+1)}{(2n+3)}[(b_0+b_{\rm ex})^{2n+3}-\{(b_0+b_{\rm ex})^{n+1}+(b_0+b_s)^{n+1}-(b_0+b_1)^{n+1}\}^{(2n+3)/(n+1)}]$$
$$+\frac{2(n+1)}{(n+2)}\{(b_0+b_{\rm ex})^{n+1}+1\}[\{(b_0+b_{\rm ex})^{n+1}+(b_0+b_s)^{n+1}-(b_0+b_1)^{n+1}\}^{(n+2)/(n+1)}-(b_0+b_{\rm ex})^{n+2}]$$
$$-b_0\{(b_0+b_s)^{n+1}-(b_0+b_1)^{n+1}\}\{2+(b_0+b_1)^{n+1}-(b_0+b_s)^{n+1}\}. \tag{A33}$$

Regime B:

$$\frac{\langle B\rangle_{\rm rem}}{B_*}=\frac{2(n+1)}{(2n+3)}\{(b_0+b_{\rm ex})^{2n+3}-(b_0+b_1)^{2n+3}\}$$
$$+\frac{2(n+1)}{(n+2)}\{(b_0+b_s)^{n+1}-1\}\left[(b_0+b_1)^{n+2}-\left\{\frac{(b_0+b_{\rm ex})^{n+1}+(b_0+b_s)^{n+1}}{2}\right\}^{(n+2)/(n+1)}\right]$$
$$+\frac{2(n+1)}{(n+2)}\{(b_0+b_{\rm ex})^{n+1}+1\}\left[\left\{\frac{(b_0+b_{\rm ex})^{n+1}+(b_0+b_s)^{n+1}}{2}\right\}^{(n+2)/(n+1)}-(b_0+b_{\rm ex})^{n+2}\right]$$
$$-b_0\{(b_0+b_s)^{n+1}-(b_0+b_1)^{n+1}\}\{2+(b_0-b_1)^{n+1}-(b_0+b_s)^{n+1}\}. \tag{A34}$$

Regime C:

$$\frac{\langle B\rangle_{\rm rem}}{B_*}=\frac{2(n+1)}{(2n+3)}[(b_0+b_{\rm ex})^{2n+3}-\{(b_0+b_s)^{n+1}-1\}^{(2n+3)/(n+1)}]$$
$$+\frac{2(n+1)}{(n+2)}\{(b_0+b_s)^{n+1}-1\}\left[\{(b_0+b_s)^{n+1}-1\}^{(n+2)/(n+1)}-\left\{\frac{(b_0+b_{\rm ex})^{n+1}+(b_0+b_s)^{n+1}}{2}\right\}^{(n+2)/(n+1)}\right]$$
$$+\frac{2(n+1)}{(n+2)}\{(b_0+b_{\rm ex})^{n+1}+1\}\left[\left\{\frac{(b_0+b_{\rm ex})^{n+1}+(b_0+b_s)^{n+1}}{2}\right\}^{(n+2)/(n+1)}-(b_0+b_{\rm ex})^{n+2}\right]-b_0, \tag{A35}$$

$$\frac{\langle B\rangle_{\rm rem\ max}}{B^*}=\frac{2(n+1)}{(2n+3)}[(b_0+b_{\rm ex})^{2n+3}-\{(b_0+b_{\rm ex})^{n+1}+1\}^{(2n+3)/(n+1)}]$$
$$+\frac{2(n+1)}{(n+2)}\{(b_0+b_{\rm ex})^{n+1}+1\}[\{(b_0+b_{\rm ex})^{n+1}+1\}^{(2n+3)/(n+1)}-(b_0+b_{\rm ex})^{n+2}]-b_0. \tag{A36}$$

Various special cases of $\langle B\rangle_{\rm rem}$ and $\langle B\rangle_{\rm in}$ have already been considered in the literature.[2,4,7,9,10,16,44–46]

[1] L. Burlachkov, Y. Yeshurun, M. Konczykowski, and F. Holtzberg, Phys. Rev. B **45**, 8193 (1992).
[2] V. V. Moshchalkov, J. Y. Henry, C. Marin, J. Rossat-Mignod, and J. F. Jacquot, Physica C **175**, 407 (1991).
[3] P. Svedlindh, K. Niskanen, P. Norling, P. Nordblad, L. Lundgren, C. Rossel, M. Sergent, R. Chevrel, and M. Potel, Phys. Rev. B **43**, 2735 (1991).
[4] R. Job and M. Rosenberg, Physica C **172**, 391 (1991).
[5] U. E. Israelson and D. M. Strayer, IEEE Trans. Magn. **MAG-27**, 1047 (1991).
[6] (a) L. Krusin-Ellbaum, A. P. Malozemoff, D. C. Cronemeyer, F. Holtzberg, John R. Clem, and Zhidong Hao, J. Appl. Phys. **67**, 4670 (1990); (b) L. Krusin-Ellbaum, A. P. Malozemoff, D. C. Cronemeyer, F. Holtzberg, G. V. Chandrashekhar, J. R. Clem, and Z. Hao, Physica A **168**, 367 (1990).
[7] M. W. McElfresh, Y. Yeshurun, A. P. Malozemoff, and F. Holtzberg, Physica A **168**, 308 (1990).
[8] L. Krusin-Ellbaum, A. P. Malozemoff, Y. Yeshurun, D. C. Cronemeyer, and F. Holtzberg, Phys. Rev. B **39**, 2936 (1989).
[9] Y. Yeshurun, A. P. Malozemoff, Y. Wolfus, E. R. Yacoby, I. Felner, and C. C. Tsuei, Physica C **162-164**, 1148 (1989).
[10] Y. Yeshurun, A. P. Malozemoff, F. Holtzberg, and T. R. Dinger, Phys. Rev. B **38**, 11 828 (1988).
[11] J. A. Hulbert, Br. J. Appl. Phys. **16**, 1657 (1965).
[12] H. Ullmaier, *Irreversible Properties of Type-II Superconductors* (Springer, New York, 1975), pp. 8–18.
[13] A. M. Campbell and J. E. Evetts, Adv. Phys. **21**, 199 (1972).
[14] J. Friedel, P. G. de Gennes, and J. Matricon, Appl. Phys. Lett. **2**, 199 (1963).
[15] S. H. Goedemoed, A. van der Giessen, D. De Klerk, and C. J. Gorter, Phys. Lett. **3**, 250 (1963).
[16] A. Echarri, Phys. Lett. **20**, 619 (1966).
[17] M. A. R. LeBlanc and D. J. Griffiths, Appl. Phys. Lett. **9**, 131 (1966).
[18] (a) Ming Xu, A. Umezawa, and G. W. Crabtree, Phys. Rev. B **46**, 11 928 (1992); (b) M. Xu, *ibid.* **44**, 2713 (1991). The B profiles displayed in these two papers are inconsistent with the critical state model and the formulas the authors develop.
[19] M. A.-K. Mohamed, J. Jung, and J. P. Franck, Phys. Rev. B **42**, 6181 (1990); **41**, 6466 (1990); **41**, 4286 (1990); **39**, 9614 (1989).
[20] Ch. J. Liu, R. Buder, C. Escribe-Filippini, J. Marcus, P. L. Raydet, B. S. Mathis, and C. Schlenker, Physica C **162-164**, 1609 (1989).
[21] D. Petitgrand, B. Gillon, A. Delapalme, G. Collin, and P. Schweiss, Physica C **162-164**, 1271 (1989).
[22] L. Fàbrega, J. Fontcuberta, B. Martinez, and S. Pinõl, Phys. Rev. B **50**, 3256 (1994).
[23] A. A. Abrikosov, Sov. Phys. JETP **5**, 1175 (1957); J. Phys. Chem. Solids **2**, 199 (1957).
[24] J. R. Clem, J. Appl. Phys. **50**, 3518 (1979).
[25] J. Silcox and R. W. Rollins, Rev. Mod. Phys. **36**, 2 (1964); Appl. Phys. Lett. **2**, 231 (1963).
[26] P. S. Swartz, Phys. Rev. Lett. **9**, 448 (1962).
[27] Yang Ren Sun, J. R. Thompson, H. R. Kerchner, D. K. Christen, M. Paranthaman, and J. Brynestad, Phys. Rev. B **50**, 3330 (1994).
[28] J. F. Bussière and V. T. Kovachev, J. Appl. Phys. **49**, 2526 (1978); J. F. Bussière and M. Suenaga, *ibid.* **47**, 707 (1976); J. F. Bussière, M. Garber, and S. Shen, Appl. Phys. Lett. **25**, 756 (1974).
[29] M. A. R. LeBlanc, G. Fillion, W. E. Timms, A. Zahradnitsky, and J. R. Cave, Cryogenics **21**, 491 (1981); M. A. R. LeBlanc and H. G. Mattes, J. Phys. (Paris) Colloq. **39**, C6-654 (1978); M. A. R. LeBlanc, D. J. Griffiths, and B. C. Bélanger, Phys. Rev. Lett. **18**, 844 (1967); M. A. R. LeBlanc and C. T. M. Chang, Appl. Phys. Lett. **10**, 344 (1967).
[30] D. G. Schweitzer and M. Garber, Phys. Rev. **160**, 348 (1967); D. G. Schweitzer and B. Bertman, *ibid.* **152**, 293 (1966).
[31] C. P. Bean and J. D. Livingston, Phys. Rev. Lett. **12**, 14 (1964).
[32] P. G. De Gennes, Solid State Commun. **3**, 127 (1965).
[33] F. Zuo, D. Vacaru, H. M. Duan, and A. M. Hermann, Phys. Rev. B **47**, 5535 (1993).
[34] P. W. Anderson and Y. B. Kim, Rev. Mod. Phys. **36**, 39 (1964).
[35] C. B. Bean, Rev. Mod. Phys. **36**, 31 (1964).
[36] M. Xu, D. Shi, and R. Fox, Phys. Rev. B **42**, 10 773 (1990).
[37] M. V. Indenbom and E. H. Brandt, Phys. Rev. Lett. **73**, 1731 (1994).
[38] N. Nakamura, G. D. Gu, and N. Koshizuka, Phys. Rev. Lett. **71**, 915 (1993).
[39] L. Burlachkov, Phys. Rev. B **47**, 8056 (1993).
[40] N. Chikumoto, M. Konczykowski, N. Motohira, and A. P. Malozemoff, Phys. Rev. Lett. **69**, 1260 (1992).
[41] M. Konczykowski, L. I. Burlachkov, Y. Yeshurun, and F. Holtzberg, Phys. Rev. B **43**, 13 707 (1991).
[42] L. Burlachkov, M. Konczykowski, Y. Yeshurun, and F. Holtzberg, J. Appl. Phys. **70**, 5759 (1991).
[43] Ming Xu, D. K. Finnemore, G. W. Crabtree, V. M. Vinokur, B. Dabrowski, D. G. Hinks, and K. Zhang, Phys. Rev. B **48**, 10 630 (1993).
[44] Z. Koziol, J. J. M. Franse, P. F. de Châtel, and A. A. Menovsky, Phys. Rev. **50**, 15 978 (1994). We note that the complicated function multiplying h in Eq. (A5) of this paper is identically unity.
[45] Y. Yeshurun, M. W. McElfresh, A. P. Malozemoff, J. Hagerhorst-Trewhella, J. Mannhart, F. Holtzberg, and G. V. Chandrashekhar, Phys. Rev. B **42**, 6322 (1990).
[46] S. F. Wahid and N. K. Jaggi, Physica C **184**, 88 (1991).
[47] M. V. Indenbom, Th. Schuster, H. Kuhn, H Kronmüller, T. W. Li, and A. A. Menovsky, Phys. Rev. B **51**, 15 484 (1995).
[48] C. A. Durán, P. L. Gammel, R. E. Miller, and D. J. Bishop, Phys. Rev. B **52**, 75 (1995).